ISPRS Journal of Photogrammetry and Remote Sensing 211 (2024) 208–227

Contents lists available at ScienceDirect

ISPRS Journal of Photogrammetry and Remote Sensing

journal homepage: www.elsevier.com/locate/isprsjprs

A Variance-Covariance method to estimating the errors of 3-D ground displacement time-series using small baseline InSAR algorithms and multi-platform SAR data

Francesco Falabella [a], Antonio Pepe [a], Angela Perrone [b,*], Tony Alfredo Stabile [b]

[a] Institute for Electromagnetic Sensing of the Environment (IREA), National Research Council (CNR) of Italy, 328 Diocleziano, Napoli 80124, Italy
[b] Institute of Methodologies for Environmental Analysis (IMAA), National Research Council (CNR) of Italy, C.da S. Loja, Tito Scalo 85050, Italy

ARTICLE INFO

Keywords:
Ground deformations
Multi-temporal SAR interferometry
Multi-sensor data combination
Variance–covariance matrices
Ground-based SAR
Landslide

ABSTRACT

The joint exploitation of complementary information from independent satellite and ground-based SAR observations can allow reconstructing the three-dimensional (up-down, east–west, north–south) ground displacement profile. Some attempts have recently been made to complement satellite and ground-based SAR (GB-SAR) data. However, a method for generating the 3-D ground displacement time-series and evaluating the quality of these estimates is still lacking. Our research aims to develop a statistical framework that is beneficial to evaluate the quality of the reconstructed 3-D ground deformation measurements achieved by jointly using space-borne and GB-SAR systems. To this purpose, the quality of multi-platform Line-of-Sight (LOS)-projected ground displacement time series is first assessed by deriving the variance–covariance matrices of noise sources (i.e., time-inconsistent phase unwrapping mistakes, decorrelation effects, and atmospheric phase screen). Subsequently, the precision of the retrieved 3-D ground displacement products is derived.

Some experiments have been performed considering the zone of Gorgoglione in southern Italy, for which three sets of SAR images are available. The first set is composed of radar images collected through a GB-SAR measurement campaign performed with the IBIS-L instrument from September 2016 to July 2017. In contrast, the spaceborne sets consist of two groups of images gathered during the same observation period by the European Copernicus Sentinel-1A/B sensors over complementary ascending (Path 146) and descending orbits (Path 124). The experimental results for the selected case-study area showed that the error bounds for the 3-D ground deformation time-series are about 3.6 mm, 3.7 mm, and 0.6 mm for the up-down, east–west, and north–south profiles, respectively.

1. Introduction

Ground subsidence is characterized by a gradual or sudden loss of the Earth's surface elevation due to natural events (Berrino et al., 1984; Boncio et al., 2010) or man-made induced processes (Gourmelen et al., 2007; Guo and Jiao, 2007). Synthetic Aperture RADAR (SAR) Interferometry (InSAR) has been proven to be an effective tool for remotely monitoring the evolution of the Earth's surface ground movements (Bamler and Hartl, 1998) with the advantage of almost total coverage of the Earth's surface. Ground displacements ascribed to natural hazard phenomena have intensely been investigated, e.g., due to earthquakes (Massonnet et al., 1993; Sandwell et al., 2000), volcano eruptions (Lundgren et al., 2003; Pritchard and Simons, 2004), landslides (Fruneau et al., 1996; Schlögel et al., 2015), permafrost freeze–thaw cycles (Daout et al., 2017; Strozzi et al., 2018; Milillo et al., 2019), and erosion (Smith et al., 2000; Liu et al., 2004), as well as, also strictly related to man-made activities, e.g., those induced by land reclamation (Ding et al., 2020; Tang et al., 2022; Zhao et al., 2022), underground mining (Samsonov et al., 2013; Yang et al., 2017), drilling tunnels (Perissin et al., 2012; Bayer et al., 2017), fossil fuel extraction and groundwater over-pumping (Erban et al., 2014; Othman and Abotalib, 2019). Thus, many InSAR methodologies have been developed to provide specific Multi-temporal InSAR (Mt-InSAR) algorithms (Hooper et al., 2004; Li et al., 2015; Dong et al., 2018; Foroughnia et al., 2019) for different

* Corresponding author.
E-mail addresses: francesco.falabella@cnr.it (F. Falabella), antonio.pepe@cnr.it (A. Pepe), angela.perrone@cnr.it (A. Perrone), tonyalfredo.stabile@cnr.it (T.A. Stabile).

https://doi.org/10.1016/j.isprsjprs.2024.04.006
Received 11 January 2024; Received in revised form 29 February 2024; Accepted 4 April 2024
Available online 12 April 2024

application contexts. The capability of the Mt-InSAR techniques to measure ground displacement with millimetric precision has widely been demonstrated in the literature (Casu et al., 2006; Ferretti et al., 2007).

It is well known that the InSAR technique can only detect the component of the ground displacement along the radar-to-target line-of-sight (LOS) direction (Wright et al., 2004). Therefore, due to the inherent limitations of measuring one-dimensional displacements along the LOS direction, a single measure cannot reconstruct the three-dimensional (3-D) components of ground deformation, leading to possible misinterpretations (Sandwell et al., 2000). As the current SAR satellites operate in sun-synchronous orbits with side-looking imaging modes, the LOS direction is nearly orthogonal to north–south (N-S), with the result that the ground displacements observed by satellite SAR systems are sensitive to movements occurring along the up-down (U-D) and east–west (E-W) directions, but they are almost insensitive to those along the north–south (N-S) direction (Wright et al., 2004; Pepe and Calò, 2017). Taking advantage of data acquired from two (ascending and descending) or more independent orbits, some methods (Samsonov and d'Oreye, 2012; Pepe et al., 2016) have been developed to combine multi-platform data that allow U-D and E-W deformations to be discriminated very accurately; however, these methods still require as an assumption that N-S pattern is somehow negligible. One way to have an estimate of ground deformations along the N-S direction is to include in the analysis the ground deformation measurements obtained along the azimuth direction using techniques such as pixel offset-tracking (POT) (Michel et al., 1999; Casu et al., 2011), multi-aperture InSAR (MAI) (Bechor and Zebker, 2006; Mastro et al., 2020) and burst-overlap interferometry (BOI) (Grandin et al., 2016). However, the problem that these estimates have much coarser precisions than those recovered through SAR interferometry persists; the overall quality of final products suffers from this lack of precision.

On the contrary, global navigation satellite system (GNSS) techniques can be combined with InSAR techniques to directly obtain three-dimensional terrain deformations at sparse spatial points, i.e., for spatial locations where both measurements are available (Gudmundsson et al., 2002; Samsonov et al., 2007). In addition, other 3-D techniques (Chen et al., 2013; Fan et al., 2021; Hu et al., 2021; Jiang et al., 2021) have been proposed in the literature. On the other hand, an attractive new opportunity in this context is provided by GB-SAR sensors, as they allow great flexibility in both sensors' positioning (within the limits of the physicality of positioning) and spatially very dense, near real-time measurements of the deformation event. It is worth noting that it is theoretically possible to position the GB-SAR sensor optimally to measure the N-S components (Wang et al., 2022). In addition, the precisions of the ground-based SAR interferometry (GB-InSAR) technique (Tarchi et al., 2003; Takahashi et al., 2013) are better than their spaceborne counterpart. Thus, exploiting both technologies to characterize ground deformation events better is possible. So far, many studies (Hilley et al., 2004; Corsini et al., 2006; Bardi et al., 2014; Carlà et al., 2018, 2019; Xiao et al., 2021) have been proposed to use interferometric SAR analyses done by both satellite and ground-based sensors to interpret better the causes and time evolution of ground deformation phenomena. Very recently, new techniques (Li et al., 2020; Di Traglia et al., 2021; Wang et al., 2022) have been proposed to combine data collected from satellite and ground-based technologies in an integrated way to benefit from the joint combination and thus obtain 3-D deformation maps. More specifically, to discern the 3-D surface displacement phase field, the method proposed by (Li et al., 2020) took advantage of the combined use of POT for satellite SAR data and interferometry for ground-based real aperture radar (RAR) data. As a result, the technique better focuses on tracking the evolution of severe deformations of the Earth's surface. In contrast, in (Di Traglia et al., 2021), the InSAR techniques were used for both satellite SAR data and ground-based SAR data to derive independent measurements of the mean ground displacement velocity, which were then jointly inverted to obtain the 3-D mean ground displacement velocity; the proposed technique was applied to follow the sin-eruptive crustal evolution of the Sciara del Fuoco (Stromboli volcano) from July 2019 to August 2019. On the same topic, steps forward moved by (Wang et al., 2022), which improved the estimated 3-D mean displacement velocity maps' reliability, developed a fine registration scheme of the space-borne and ground-based images and adopted a weighted inversion of the InSAR phases to achieve the 3-D displacement field.

However, retrieving 3-D ground displacement time series jointly using satellite and ground-based SAR sensors is still unexplored. Strictly related to the reliability of the retrieved 3-D measurements, there is a complete lack of a statistical treatment for quantifying the composite effect of uncertainty signals that degrade the precisions of the obtained three-dimensional ground displacement time series.

In this study, we present and analyze the performance of a multi-platform SAR combination method for deriving 3-D ground mean displacement velocity maps and ground displacement time series by employing satellite and GB-SAR data. A comprehensive analysis of stochastic effects is performed, considering the time-inconsistent phase unwrapping errors and the decorrelation noise sources. Thus, a method for quantifying the precision of each measured 3-D ground deformation field is provided, and synthetic indicators of the reliability of the computed ground displacement products related to coherent scatterers, which consider the entire 3-D covariance matrix, are also presented.

The developed statistical framework was tested on a real case considering a SAR dataset collected by satellite and ground-based instruments of the Gorgoglione town in southern Italy to shed light on the expected experimental accuracies in estimating and characterizing the three-dimensional surface motions. During the analysis period, the selected test site was affected by a slow landslide that produced a subtle spatiotemporal ground deformation, for which a displacement in the N-S direction and, more generally, in the 3-D field was suspected. The experimental results confirm the 3-D displacement of the slow-varying landslide, highlighting the crucial role of the integrated use of satellite and terrestrial SAR platforms, from which the ground displacement components blind to the ascending and descending satellite orbits were also recovered. The retrieved ground deformations are also in agreement with the geomorphological nature of the landslide itself. In addition, the developed 3-D statistical framework provides better accuracies for U-D and E-W sensing than those obtainable using only satellite datasets; it also provides submillimeter accuracies for N-S sensing.

The remainder of this article is organized as follows. Section 2 presents and describes the methods adopted to obtain the InSAR 3-D ground displacement products. Section 3 details the statistical framework adopted for assessing the quality of 3-D ground displacement time series. Section 4 describes the real case of the Gorgoglione landslide and the multi-platform SAR data. Experimental results for estimating the 3-D ground deformation field, supported by an analysis of the detected ground motions and applying the developed statistical framework, are presented in Section 5. Discussions and conclusions are finally addressed in Sections 6 and 7, respectively.

2. Methodologies

In this Section, we focus on a method for the generation of 3-D ground displacement products starting from sequences of SAR images collected through multi-viewing (ascending/descending) satellite orbital passes and using one (or more) GB-SAR instrument that observes the same scene on slightly the same days (i.e., we assume the available multi-platform SAR acquisitions are almost time synchronous). The independently generated LOS-projected ground displacement time series are thus combined to discriminate the three-dimensional (3-D) components of ground deformation. Applying the noise propagation laws (Birge, 1939; Goodman, 1960; Ku, 1966), we finally assess the precision of the retrieved 3-D ground displacement time series for every acquisition time and determine synthetic parameters that characterize the error of the generated 3-D products.

2.1. Joint exploitation of terrestrial and spaceborne SAR system for the retrieval of 3-D mean ground displacement velocity maps

Let us start our analysis by assuming the availability of three independent sets of SAR data acquired from satellite radar systems with complementary viewing geometries and one (or more) terrestrial radar instrument. The first two groups are composed of N_1 and N_2 images collected at the acquisition times $\left[t_{0,i}, t_{1,i}, ..., t_{N_i-1,i}\right]^T$ $i = 1, 2$ through ascending and descending orbits, respectively. The third set is composed of N_3 images collected at $\left[t_{0,3}, t_{1,3}, ..., t_{N_3-1,3}\right]^T$ by a GB-SAR instrument. Note that T stands for the transpose operation. With respect to satellite systems of observations, the terrestrial instruments can operate over the overlapped period between the ascending and descending SAR passes and are characterized by a time series of data with enhanced sampling times, from the weekly repetition times of satellite systems to the hourly rates or less of the GB-SAR systems. Also, GB-SAR instruments collect images with higher spatial resolutions than those from space (see Table 1). The three sets of SAR data are preliminarily independently processed to obtain the LOS-projected ground displacement time-series $\mathbf{l}_i(P) = \left[l_{0,i}(P), l_{1,i}(P), ..., l_{N_i-1,i}(P)\right]^T \ \forall P \in \mathrm{Y}_i;\ i = 1, 2, 3$ and the corresponding mean displacement velocity maps $v_i(P),\ i = 1, 2, 3$ in correspondence with a group of coherent, well-processed points Y_i. The latter can be identified by computing the temporal coherence γ_i from the obtained deformation time series and applying a proper threshold $\mathrm{Y}_i \equiv \{P : \gamma_i(P) \geq \gamma_{thres}\}$. We remark that the temporal coherence factor was initially proposed by (Pepe and Lanari, 2006), and since then, it has widely been applied in several contexts (Tizzani et al., 2007; Lauknes et al., 2011; Cigna and Tapete, 2021; Izumi et al., 2022b). It relies on the computation of the ground displacement time series. In particular, considering the i-*th* given SAR dataset, the process that leads to generating the ground displacement time series from a set of M_i unwrapped multi-temporal SAR interferograms $\Delta\Phi_i = \left[\Delta\phi_{0,i}, \Delta\phi_{1,i}, ..., \Delta\phi_{M_i-1,i}\right]^T$ can be seen as the solution of the following system of linear equations:

$$\mathbf{B}_i \bullet \boldsymbol{g}_i = \Delta\Phi_i \tag{1}$$

where $\mathbf{B}_i$ is the design matrix of the considered linear transformation, and $\boldsymbol{g}_i$ is the model of Q unknown parameters that characterize the ground deformations, e.g., the velocities between consecutive time acquisitions in the implementation provided within the SBAS method (Berardino et al., 2002).Also, the symbol $\cdot$ stands for the matrix multiplication (rows by columns) operator. The temporal coherence is thus obtained by extracting the residuals of the linear transformation $\boldsymbol{r}_i = \mathbf{B}_i \bullet \boldsymbol{g}_i - \Delta\Phi_i$ and using them to compute the following factor:

$$\gamma_i = \frac{1}{M_i}\left|\sum_{m=0}^{M_i-1} exp[jr_m]\right| \tag{2}$$

where $j = \sqrt{-1}$ is the imaginary unit.

To ensure the high capabilities in terms of spatial resolutions offered by the GB-SAR systems, the relative single-look (SL) InSAR products are more profitably computed. Specifically, in our work, the multi-grid InSAR approach proposed by (Falabella et al., 2022b) is employed to generate full-resolution ground displacement time series. Alternative methods for generating ground displacement time series of coherent targets can also be adopted.

The full-resolution unwrapped phases are then used to get the LOS ground displacement time series by solving the system of linear equations (1). It is worth noting that the vector of unwrapped phases $\Delta\Phi_i$ is contaminated by other contributions that can be treated as spurious terms with respect to the (true) deformation signals. A standard model used in literature is $\Delta\Phi_i = \Delta\Phi_i^{displ} + \Delta\Phi_i^{r\_topo} + \Delta\Phi_i^{r\_orbits} + \Delta\Phi_i^{APS} + \Delta n_i$ (Bamler and Hartl, 1998; Mora et al., 2003; Pepe and Calò, 2017); $\Delta\Phi_i^{displ}$ the displacement phases, $\Delta\Phi_i^{r\_topo}$ the residual-topography-induced phases due to inaccuracies in the Digital Elevation Model (DEM), $\Delta\Phi_i^{r\_orbits}$ the residual phases accounting for inaccurate orbital information, $\Delta\Phi_i^{APS}$ the atmospheric phase screen (APS) contributions due to the change in the tropospheric and ionospheric dielectric constant, and Δn_i the decorrelation noise sources (Zebker and Villasenor, 1992). Furthermore, additional uncertainties come out when phase unwrapping errors are committed. Hence, the estimated displacement time series are affected by the presence of uncertainty components that influence the precision of the calculated values.

We remark that the residual topography, the artefacts related to imprecise orbital information as well as the tropospheric APS contributions (which are correlated to the surface height profile) can be estimated and properly compensated for using the *ad-hoc* refinement procedures that are implemented in the specific Mt-InSAR processing chains (e.g., Berardino et al., 2002; Mora et al., 2003, etc.). To emphasize the role of major error sources, which are linked to random decorrelation noise and PhU mistakes, hereinafter we explicitly assume that these phase artefacts have already been compensated for in the computed sequence of unwrapped interferograms. Interested readers can refer to the literature to have additional details on the procedures adopted to perform such compensations (Samsonov, 2010; Fattahi and Amelung, 2013; Bekaert et al., 2015; Tian et al., 2018; Du et al., 2021; Liang et al., 2023). We also remark there is a maximum measurable spatial deformation gradient with SAR interferometry techniques, which is equal to one fringe per pixel or, equivalently, half the wavelength per pixel (Massonnet and Feigl, 1998; Baran et al., 2005). In practice, (complete) incoherence occurs when this limit condition (a fringe per pixel) is reached; in this case, the interferometric phase turns out to be uniformly distributed and phase unwrapping miserably fails.

Under these assumptions, the uncertainties of the ground deformation measurements can be accounted for by the knowledge of the covariance matrix of the LOS-projected ground displacement measurements, and by taking into account the basic rules of error propagation (Ku, 1966), as follows:

$$\begin{aligned}\mathbf{C}_{g_i} &= \mathbf{B}_i^{\dagger} \bullet \mathbf{C}_{\Delta\Phi_i} \bullet \mathbf{B}_i^{\dagger T} \\ &\cong \mathbf{B}_i^{\dagger} \bullet \mathbf{C}_{n_i} \bullet \mathbf{B}_i^{\dagger T} + \mathbf{B}_i^{\dagger} \bullet \mathbf{C}_{PhU_i} \bullet \mathbf{B}_i^{\dagger T} + \mathbf{B}_i^{\dagger} \bullet \mathbf{C}_{turb\_APS_i} \bullet \mathbf{B}_i^{\dagger T}\end{aligned} \tag{3}$$

where $\mathbf{C}_{\Delta\Phi_i}$ represents the covariance matrix of the unwrapped interferometric SAR phases, $\mathbf{B}_i^{\dagger}$ is the pseudoinverse of the design matrix, and T stands for the matrix transposition operator. Note that in Eq. (3), $\mathbf{C}_{\Delta\Phi_i}$ is modelled with a sum of three distinct and independent uncertainty contributions, namely, $\mathbf{C}_{n_i}$ related to the decorrelation sources, $\mathbf{C}_{PhU_i}$ related to PhU errors committed during the signal processing stages, and $\mathbf{C}_{turb\_APS_i}$ associated with the effect of the turbulent APS components. By assuming PhU errors are independent and identically distributed (i.i.d), the simpler homoscedastic (Ramsey, 1969) case first holds:

$$\mathbf{C}_{PhU,i} = \sigma_{PhU,i}^2 \mathbf{I} \tag{4}$$

where $\mathbf{I} \in \mathbb{R}^{M_i \times M_i}$ is the identity matrix, and $\sigma_{PhU,i}^2$ is the variance of PhU errors related to the i-*th* SAR dataset. The latter term can effectively be computed using directional statistics (Mardia and Jupp., 1999) and the value of temporal coherence factor (see Eq. (2)). This derivation represents one of the innovation points raised in our work. Indeed, the i-*th* temporal coherence factor γ_i represents the resultant mean length of the wrapped residuals between the original interferograms and those reconstructed from the generated *i-th* LOS-projected ground displacement time series. Since this analysis is carried out at the single look scale, one can demonstrate that these phase residuals only account for time inconsistent PhU mistakes (Pepe, 2021). Under the simplified

homoscedastic assumption, these phase terms can also be assumed distributed as wrapped normal[1] (Collett and Lewis, 1981) $WN = (\mu_i, \gamma_i)$ and $\sigma^2_{PhU,i} = -2\ln\gamma_i$.

The retrieved ground surface displacement time series and the mean displacement velocity maps are finally georeferenced to a common geographical reference geometry for further analysis. Then, over the group of points that are coherent on all three datasets, the LOS-projected ground displacement velocity values can be combined to discriminate the 3-D components [i.e., up-down (v_{up}), east–west (v_{east}), north–south (v_{north})] of the ground deformations (Pepe and Calò, 2017; Di Traglia et al., 2021) as follows:

$$v_i = -\sin\vartheta_i\cos\varphi_i v_{east} + \cos\vartheta_i v_{up} - \sin\vartheta_i\sin\varphi_i v_{north} \tag{5}$$

where, considering the adopted multi-platform dataset and configuration (e.g., for $i = 1, 2, 3$), v_i represents the LOS mean displacement velocity value, with ϑ_i and φ_i being the incidence and the satellite heading angles, respectively. A pictorial representation of the generic multi-platform 3-D geometry is sketched in Fig. 1. The 3-D domain has been subdivided into two bi-dimensional sub-domains highlighting the LOS directions and the relative angles of interest for every single SAR sensor.

Thus, Eq. (5) leads to the following system of linear equations: $\mathbf{A}_v \bullet \mathbf{V}_{3-D} = \mathbf{V}_{LOS}$, where $\mathbf{A}_v \in \mathbb{R}^{3\times3}$ is the design matrix, $\mathbf{V}_{3-D} = \left[v_{up}, v_{east}, v_{north}\right]^T$ is the vector of unknows, and $\mathbf{V}_{LOS} = \left[v_1, v_2, v_3\right]^T$ is the vector of measures.

Moreover, ground-based measurements are generally more reliable (Tarchi et al., 2003; Takahashi et al., 2013) than their satellite counterparts because of less temporal and geometric decorrelation and the much smaller wavelength characterizing transmitted and received electromagnetic waves. Notably, in zero perpendicular spatial baseline configuration, the effects related to the physical separation between acquisitions are absent, e.g., the geometrical decorrelation (Bamler and Hartl, 1998). Indeed, the zero-baseline configuration is usually adopted when GB-SAR systems are employed for InSAR displacement field estimation purposes (Leva et al., 2003; Monserrat et al., 2014).

2.2. 3-D ground displacement time series generation

This subsection addresses the generation of 3-D ground displacement time series in a quasi-synchronous scenario when available SAR images are acquired (roughly) on the same day for all terrestrial and spaceborne platforms. Accordingly, the intersection between the sets of the acquisition times related to the two satellite orbits is considered $\mathbf{t}_{SAT} = \left\{\left[t_{0,i=1}, t_{1,i=1}, \ldots, t_{N_1-1,i=1}\right]^T \cap \left[t_{0,i=2}, t_{1,i=2}, \ldots, t_{N_2-1,i=2}\right]^T\right\}$, $i = 1, 2$. Note that we considered (at most) an offset of one day from ascending and descending acquisition times, fulfilling the simplified quasi-synchronous hypothesis. Similarly, considering the GB-SAR acquisitions, for $i = 3$, the set of quasi-synchronous acquisition times is identified as $\mathbf{t}_{SYNC} = \left\{\mathbf{t}_{SAT} \cap \left[t_{0,i=3}, t_{1,i=3}, \ldots, t_{N_3-1,i=3}\right]^T\right\} = \left[t_0^{(SYNC)}, t_1^{(SYNC)}, \ldots, t_{N_{SYNC}-1}^{(SYNC)}\right]^T \in \mathbb{R}^{N_{SYNC}}$ with N_{SYNC} the number of quasi-synchronous acquisitions.

The vector of quasi-synchronous acquisition times $\mathbf{t}_{SYNC}$ highlights effectively only the temporal samples where both multi-platform measures are present, avoiding the use of interpolating procedures. The multi-platform vectors of LOS ground displacement time series $\mathbf{l}_i$, for $i = 1, 2, 3$, are extracted in correspondence with acquisition times $\mathbf{t}_{SYNC}$. Note that, for the GB-SAR vector $\mathbf{l}_3$ only, all LOS measurements within each synchronous daily time instant were averaged to obtain a single daily measurement without losing the benefits of the GB-SAR instrument dense temporal sampling and enhancing signal-to-noise ratio (SNR) of the 3-D ground displacement measurements.

[1] The wrapped normal distribution is obtained by wrapping the normal distribution onto the unitary circle.

Thus, similarly to (5), the synchronous 3-D surface displacement time series is achieved for every coherent SAR pixel imaged by the different SAR instruments by solving the following determined system of linear equations:

$$\mathbf{A}_d \bullet \begin{bmatrix} \mathbf{d}_{east} \\ \mathbf{d}_{up} \\ \mathbf{d}_{north} \end{bmatrix} = \begin{bmatrix} \mathbf{l}_1 \\ \mathbf{l}_2 \\ \mathbf{l}_3 \end{bmatrix} \tag{6}$$

where $\mathbf{A}_d \in \mathbb{R}^{3N_{SYNC}\times3N_{SYNC}}$ is the design matrix, and $\begin{bmatrix} \mathbf{d}_{east} \\ \mathbf{d}_{up} \\ \mathbf{d}_{north} \end{bmatrix} \in \mathbb{R}^{3N_{SYNC}\times1}$ is the vector of (unknown) 3-D surface displacement time-series. For instance, if we consider the case when $N_{SYNC} = 2$, the design matrix $\mathbf{A}_d$ is as follows

$$\mathbf{A}_d = \begin{bmatrix} -\sin\vartheta_1\cos\varphi_1 & 0 & \cos\vartheta_1 & 0 & -\sin\vartheta_1\sin\varphi_1 & 0 \\ 0 & -\sin\vartheta_1\cos\varphi_1 & 0 & \cos\vartheta_1 & 0 & -\sin\vartheta_1\sin\varphi_1 \\ \sin\vartheta_2\cos\varphi_2 & 0 & \cos\vartheta_2 & 0 & -\sin\vartheta_2\sin\varphi_2 & 0 \\ 0 & \sin\vartheta_2\cos\varphi_2 & 0 & \cos\vartheta_2 & 0 & -\sin\vartheta_2\sin\varphi_2 \\ -\sin\vartheta_3\cos\varphi_3 & 0 & \cos\vartheta_3 & 0 & -\sin\vartheta_3\sin\varphi_3 & 0 \\ 0 & -\sin\vartheta_3\cos\varphi_3 & 0 & \cos\vartheta_3 & 0 & -\sin\vartheta_3\sin\varphi_3 \end{bmatrix} \in \mathbb{R}^{6\times6}$$

In addition, the addressed problem can also be extended to asynchronous scenarios benefiting from the heterogeneous temporal samplings of different multi-platform sources (Wright et al., 2004; Samsonov et al., 2007; Pepe et al., 2016). Fig. 2 highlights the flow chart for generating the 3-D ground displacement time series discussed in Section 2.

3. Variance-Covariance matrices of the 3-D ground displacement products

The mathematical treatment of the terms constituting the uncertainty relation expressed in Eq. (3) and the evaluation of their effects on the estimated 3-D InSAR ground displacement products are fully addressed hereinafter.

3.1. Decorrelation noise effects

The characterization of the "true" InSAR covariance matrix $\mathbf{C}_{n_i}$ has been treated in several independent works (Tough et al., 1995; Bamler and Hartl, 1998; Rocca, 2007; De Zan et al., 2015; Agram and Simons, 2015). Precisely, (Tough et al., 1995; Bamler and Hartl, 1998) held the simplified assumption of zero correlation between different InSAR phases, and the InSAR variances were directly evaluated in closed form by solving the non-trivial integral forms (Tough et al., 1995), also known the precise expression of the marginal Probability Density Function (PDF) of the interferometric phases (Lee et al., 1994). Instead, decorrelation models are employed in (Rocca, 2007; De Zan et al., 2015; Agram and Simons, 2015) to find covariance expressions that also consider the correlation among the different interferograms. Recently, by relaxing the assumption that complex interferograms have a complex circular Gaussian (CCG) distribution [as assumed in (Rocca, 2007; De Zan et al., 2015)] and proposing an alternative model of surface decorrelation, more general forms of covariance were presented in (Samiei-Esfahany and Hanssen, 2017) and (Zheng et al., 2021), respectively.

Using the covariance expressions proposed in (Rocca, 2007; De Zan et al., 2015) for populating the "true" unwrapped InSAR covariance matrix, and referring to a generic interferometric couple $\Delta\phi_{ef}$ and $\Delta\phi_{xy}$, where e, f, x, y highlight the SAR image indexes, the following expression for the covariance matrix elements is thus obtained:

$$\mathrm{cov}\left\{\Delta\phi_{ef}, \Delta\phi_{xy}\right\} = \frac{\zeta_{ey}\zeta_{fx} - \zeta_{ef}\zeta_{xy}}{2L\zeta_{ef}\zeta_{xy}} \tag{7}$$

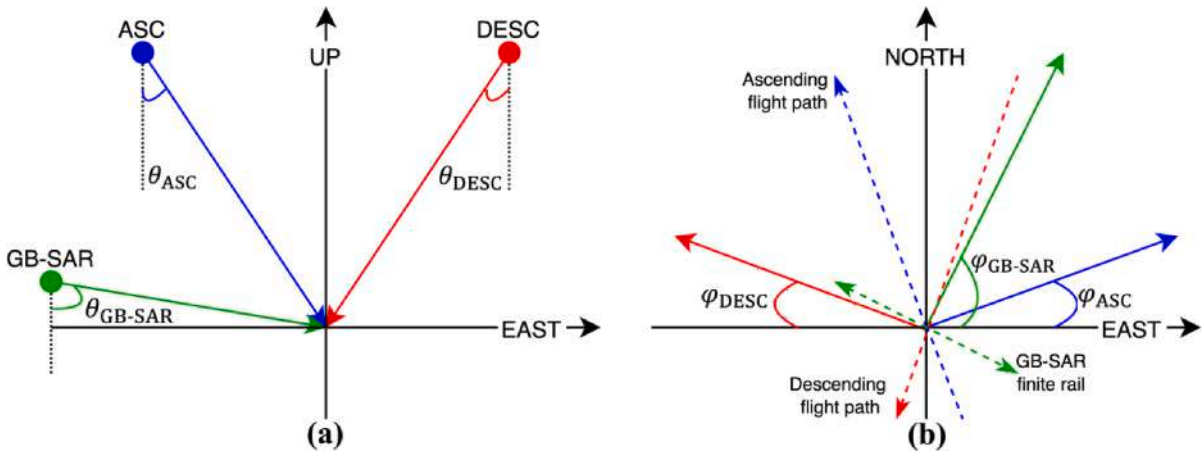

Fig. 1. Pictorial representation of a multi-platforms 3-D SAR geometry, where are highlighted the ascending (ASC) and descending (DESC) satellite LOS geometries, and also the terrestrial (GB-SAR) LOS geometry. a) Projection in the East-Up 2-D plane. b) Projection in the East-North 2-D plane.

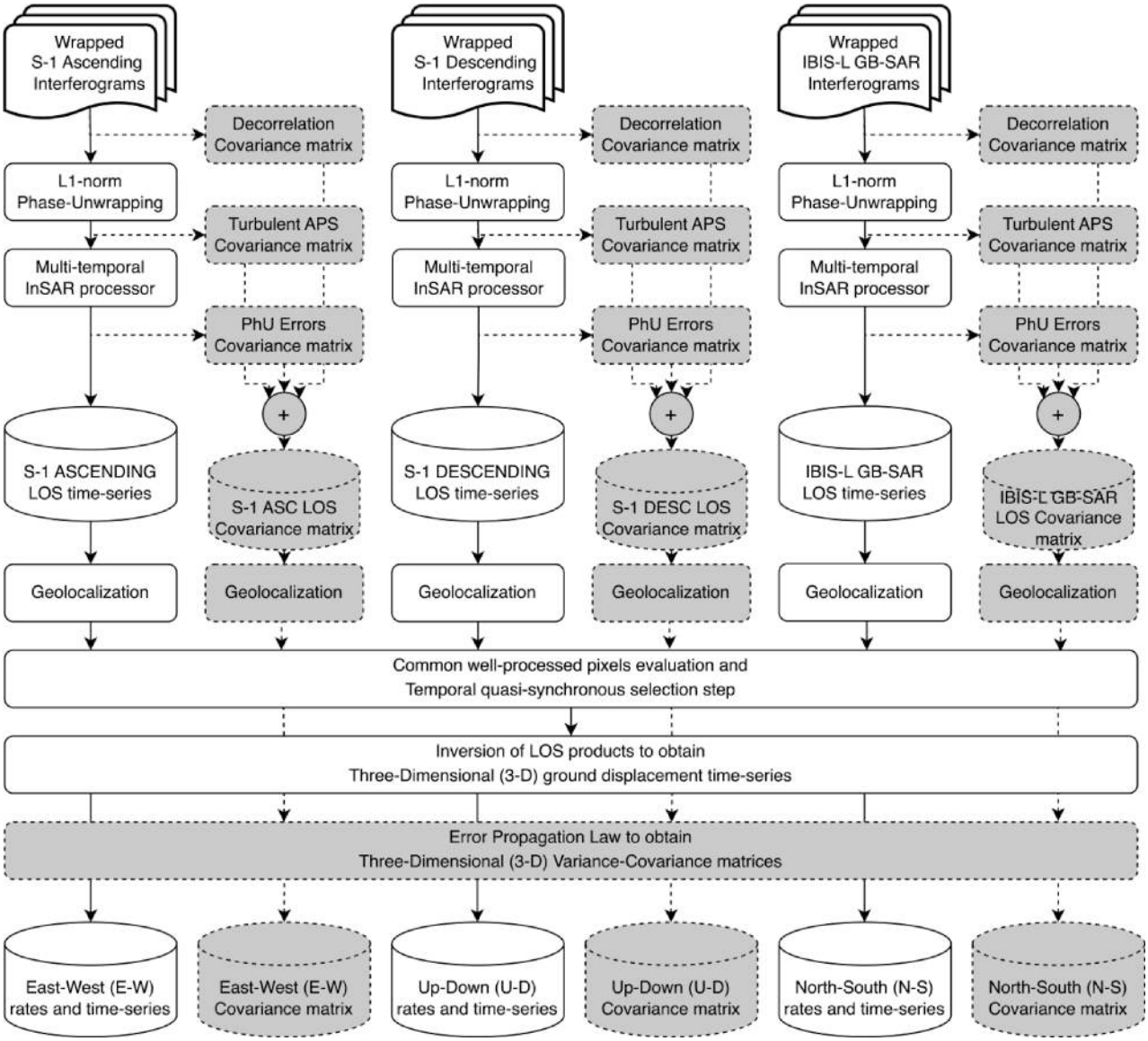

Fig. 2. Flow chart of the developed methodology for estimating multi-platform 3-D ground displacement time-series and their covariance matrices. White shapes and solid lines highlight the flow for calculating InSAR 3-D multi-platform products, while grey and dashed lines refer to the statistical error framework.

where ζ_{ey} are the coherence magnitudes, and L is the number of independent looks. Note that when the condition $e = x$ and $f = y$ holds the covariance expression in (7) particularizes to the well-known Cramér-Rao bound for the interferometric phases; as a consequence, the diagonal elements of the full covariance matrix have the following expression: $\mathrm{cov}\left\{\Delta\phi_{xy}, \Delta\phi_{xy}\right\} = \mathrm{var}\left\{\Delta\phi_{xy}\right\} = \frac{1-\zeta_{xy}{}^2}{2L\zeta_{xy}{}^2}$. The expression in (7) is valid for characterizing distributed scatterers (DS) that do not have any prevalent contributions among individual scatterers in the resolution cell and under the assumption of CCG distribution of complex interferograms. Further, the CCG assumption has been relaxed (Samiei-Esfahany and Hanssen, 2017), and the following generalization of (7) is achieved:

$$\mathrm{cov}\left\{\Delta\phi_{ef}, \Delta\phi_{xy}\right\} = \frac{\zeta_{ex}\zeta_{fy} - \zeta_{ey}\zeta_{fx}}{2L\zeta_{ef}\zeta_{xy}} \tag{8}$$

Insofar as the formula in (7) also uses mutual coherence magnitudes with respect to the intrinsic coherences of the interferograms for which covariance is being calculated, the counterpart in (8) uses all possible coherences that can be calculated from the combination of the indices forming the two interferograms for which covariance is being calculated, so (8) is more general than (7). Moreover, both (7) and (8) involve the use of all generable interferometric pairs and thus are particularly suitable for characterizing the covariances of interferograms when using approaches that treat DSs in a complementary PS-like manner (Guarnieri and Tebaldini, 2008; Ferretti et al., 2011; Fornaro et al., 2015; Ansari et al., 2018). Elsewhere, covariance statistical expressions that account for only a reduced set of interferograms, for instance, by following the small baseline paradigm (Berardino et al., 2002; Mora et al., 2003; Casu et al., 2006; Even and Schulz, 2018), are absent. Counterintuitively, the relation in (7) or (8) could be used.

A strategy for expressing the decorrelation covariance terms $\mathbf{C}_{n_i}$ that relies exclusively on the used small baseline (SB) InSAR pairs is proposed in our work and described hereinafter. The procedure takes advantage of the fundamental properties of directional statistics (Mardia and Jupp., 1999). More generally, the directional circular vector of the wrapped InSAR phases $\Delta\Phi_i = \left[\Delta\phi_{0,i}, \Delta\phi_{1,i}, ..., \Delta\phi_{M_i-1,i}\right]^T$, for $i = 1, 2, 3$, can be assumed distributed according to a multi-samples von Mises distribution $VM(\boldsymbol{\mu}_i, \boldsymbol{\kappa}_i)$ (Mardia and Jupp., 1999), where $\boldsymbol{\mu}_i$ and $\boldsymbol{\kappa}_i$ are the multi-sample vectors of the means and concentration parameters, respectively. Basically, the wrapped phases result from the superposition of L independent random samples within the resolution cell Θ: $\Delta\phi_{m,i} = \measuredangle\left\{\frac{1}{L}\sum_{\Theta} exp\left[j\Delta\phi_{m,i}^{(\Theta)}\right]\right\}$, for $m = 0, 1, ..., M_i - 1$ and $i = 1, 2, 3$. Likewise, the sine and cosine of wrapped InSAR phases can have zero-mean multi-samples von Mises distributions $VM\left(0, \boldsymbol{\kappa}_{sin,i}\right)$ and $VM\left(0, \boldsymbol{\kappa}_{cos,i}\right)$, for the sine $S_{m,i} = \sum_{\Theta}\sin\left[\Delta\phi_{m,i}^{(\Theta)}\right]$ and cosine $C_{m,i} = \sum_{\Theta}\cos\left[\Delta\phi_{m,i}^{(\Theta)}\right]$ terms, respectively. Hence, following the statistical assumptions now adopted, it can be demonstrated that for high-concentration parameters $\boldsymbol{\kappa}_i$ (Mardia and Jupp., 1999), the interferometric variance terms can be characterized as follows:

$$\mathrm{var}\left\{\Delta\phi_{m,i}\right\} \approx \frac{1}{L\kappa_{m,i}}\left(1 + \frac{1}{2\kappa_{m,i}}\right) \tag{9}$$

Let us now derive the covariance between the two generic interferograms α, i and β, i of the *i-th* interferometric SAR dataset. We observe that:

$$\mathrm{cov}\left\{\Delta\phi_{\alpha,i}, \Delta\phi_{\beta,i}\right\} = \frac{1}{2}\mathrm{var}\left\{\Delta\phi_{\alpha,i}\right\} + \frac{1}{2}\mathrm{var}\left\{\Delta\phi_{\beta,i}\right\} - \frac{1}{2}\mathrm{var}\left\{\Delta\phi_{\alpha,i} - \Delta\phi_{\beta,i}\right\} \tag{10}$$

Accordingly, from Eqs. (9) and (10), the relevant covariance value is finally achieved as:

$$\mathrm{cov}\left\{\Delta\phi_{\alpha,i}, \Delta\phi_{\beta,i}\right\} = \frac{1}{2L}\left[\frac{1}{\kappa_{\alpha,i}}\left(1 + \frac{1}{2\kappa_{\alpha,i}}\right) + \frac{1}{\kappa_{\beta,i}}\left(1 + \frac{1}{2\kappa_{\beta,i}}\right) - \frac{1}{\kappa_{\alpha\beta,i}}\left(1 + \frac{1}{2\kappa_{\alpha\beta,i}}\right)\right] \tag{11}$$

where suitable expansions of the following function $A(\boldsymbol{\kappa}_i) = I_1(\boldsymbol{\kappa}_i)/I_0(\boldsymbol{\kappa}_i)$ (defined as the ratio of modified Bessel functions of the first kind and first $[I_1(\cdot)]$ and zero $[I_0(\cdot)]$ order) is required for a feasible computation of the concentration parameters $\boldsymbol{\kappa}_i$ (Mardia and Jupp., 1999). Likewise, maximum likelihood estimates (MLE) of the concentration parameters $\widehat{\boldsymbol{\kappa}}_i$ in (11) can be obtained, for instance, by using one of the approximations proposed in (Dobson, 1978), and in particular, the following formula can be adopted:

$$\widehat{\kappa}_{m,i} \approx \left(1.28 - 0.53\widehat{\rho}_{m,i}^2\right)\tan\left(\frac{\pi\widehat{\rho}_{m,i}}{2}\right) \tag{12}$$

where $\widehat{\rho}_{m,i} = \left|\frac{1}{L}\sum_{\Theta}\exp\left[j\Delta\phi_{m,i}^{(\widehat{\Theta})}\right]\right|$ is the mean resultant length of the m-th wrapped InSAR phases of the i-th InSAR dataset. It is computed assuming the ergodicity condition and calculating the MLEs considering a group of pixels nearby a given SAR pixel enclosed by the spatial box $\widehat{\Theta}$. It is worth noting that, the jointly maximum likelihood concentration parameter $\widehat{\kappa}_{\alpha\beta,i}$ in (11) is always obtained using (12), taking into account the following mean resultant length $\widehat{\rho}_{\alpha\beta,i} = \left|\frac{1}{L}\sum_{\Theta}\exp\left[j\left(\Delta\phi_{\alpha,i}^{(\widehat{\Theta})} - \Delta\phi_{\beta,i}^{(\widehat{\Theta})}\right)\right]\right|$. The adopted directional-based statistical formalism can be applied to characterizing DS and PS targets.

3.2. Time-Inconsistent PhU errors and atmospheric phase disturbances

The focus is now posed on the analysis of the covariance matrix related to PhU errors, i.e., $\mathbf{C}_{PhU_i}$, and, in particular, only on those related to time-inconsistent errors (Pepe, 2021; Falabella and Pepe, 2022) that produce non-zero phase residuals[2] when the linear system of equations (1) is solved. A rigorous characterization of the PhU errors covariance matrix is utterly absent in the literature because several critical points must jointly be addressed, thus preventing the straightforward evaluation of PhU errors in any possible closed form. One of these crucial points is the absence of any PDF for characterizing unwrapped phases, especially for PhU errors, both consistent and inconsistent in time. Then, there is a lack of methods for quantifying the PhU errors for each unwrapped interferometric phase. Elsewhere, time-inconsistent PhU errors have been known to cause phase residuals minimizing for (1), but the residuals can also be ascribed to other effects, both stochastics and systemic (Falabella and Pepe, 2022; Maghsoudi et al., 2022; Zheng et al., 2022), such as the recently observed fading signal (Ansari et al., 2021).

Moreover, it is worth noting that when the single-look scenario is considered, the residuals that result from solving the problem in (1) are exclusively related to the time-inconsistent PhU errors. Globally, the latter residuals afflict the estimated InSAR displacement field product reliability. Therefore, we propose to apply a method to calculate a proxy for characterizing the variance–covariance matrix of time-inconsistent PhU errors using least-squares (LS) residuals (Anscombe and Tukey, 1963). The procedure is valid for achieving the final covariance matrix of the 3-D ground displacement time series. Still, it is somehow not wholly rigorous for characterizing the covariances of each PhU error for each interferogram because the LS solution tends to spread PhU errors made on every single interferogram over the entire network of the interferogram, so the residuals cannot be directly related to PhU errors on individual interferograms. Still, instead, they reflect well the overall

[2] Note that any operation that is independently performed on every SAR acquisitions does not lead to temporal phase inconsistencies and accordingly does not produce phase residuals.

effect of these errors on the obtained ground displacement time series.

Referring to the single-look case analysis and in the presence of time-inconsistent PhU errors, the system of linear equations (1) can be expressed in a complementary way:

$$\mathbf{B}_i \bullet \boldsymbol{g}_i + \boldsymbol{\varepsilon}_i = \Delta\Phi_i \tag{13}$$

where $\mathbf{B}_i$ is the design matrix, $\boldsymbol{g}_i$ is a model of unknown parameters that characterize the ground deformations, $\Delta\Phi_i$ are the unwrapped InSAR phases, and $\boldsymbol{\varepsilon}_i$ is the vector of committed PhU errors. The Gauss–Markov theorem (Shaffer, 2012) asserts that $\widehat{\boldsymbol{g}}_i = \left(\mathbf{B}_i{}^T\mathbf{B}_i\right)^{-1}\mathbf{B}_i{}^T\Delta\Phi_i = \mathbf{B}_i^{\dagger}\Delta\Phi_i$ is the best linear unbiased estimator (BLUE) of $\boldsymbol{g}_i$ and it is obtained by solving (13) in the ordinary least-squares (OLS) sense under the assumption of homoscedasticity of the error vector $\boldsymbol{\varepsilon}_i$ (Ramsey, 1969). The homoscedastic condition holds when the PhU errors are assumed to be zero-mean i.i.d., and therefore, the simplified statistical treatment exposed in the previous Sections easily applies, i.e., a unique variance value is enough for characterizing the diagonal elements of the PhU errors covariance matrix [see Eq. (4)]. The assumption that PhU errors are i.i.d. normal is not generally enough, and it is easy to demonstrate its untruthfulness practically as well. In fact, using consolidated 2-D phase unwrapping algorithms (Goldstein et al., 1988; Ghiglia and Romero, 1994; Pritt, 1996; Costantini, 1998) the interferograms are independently unwrapped, and the committed PhU errors can be treated as independent, but they are not necessarily identically distributed. As a result, the covariance matrix of PhU errors is diagonal, but the diagonal elements of the matrix are different, i.e., the vector of errors $\boldsymbol{\varepsilon}_i$ can be considered heteroscedastic (Ramsey, 1969). The same outcomes are also plausible when adopting well-known hybrid 2-D + 2-D approaches (Pepe and Lanari, 2006; Fornaro et al., 2011). Instead, pure 3-D techniques (Hooper and Zebker, 2007; Shanker and Zebker, 2010; Costantini et al., 2012) fully exploit both temporal and spatial relationships for the PhU process, so the computation of the full covariance matrix is mandatory.

Moreover, LS phase residuals are absent when pure 3-D approaches are employed. As a result, it is impossible to discriminate PhU errors, which are, to some extent, inevitable. Other specialized strategies must be developed to discover the committed PhU errors that cannot be identified by checking the unwrapped phases' temporal consistency and remaining practically "hidden". Hereafter, the covariance matrix of time-inconsistent PhU errors in case of heteroscedasticity, adopting LS phase residuals $\widehat{\boldsymbol{\varepsilon}}_i$ (Anscombe and Tukey, 1963) to obtain a proxy for covariances is addressed. The adopted framework is derived from numerous studies in econometrics, which have thoroughly investigated the problems of errors heteroscedasticity by proposing efficient and robust estimators of the heteroscedasticity consistent covariance matrix (HCCM) (White, 1980; MacKinnon and White, 1985; Freedman, 2006). The concept behind the HCCM estimator is to use the squared LS phase residuals $\widehat{\boldsymbol{\varepsilon}}_i^2$ to estimate the diagonal entries of the PhU errors covariance matrix $\mathbf{C}_{PhU_i}$, i.e., the variance values of the time-inconsistent PhU errors. The most widely used form of HCCM estimator is proposed by (White, 1980) and can be thought of as estimating the variances of $\boldsymbol{\varepsilon}_i$ with a single observation:

$$\mathbf{C}_{PhU_i} = diag\left[\widehat{\boldsymbol{\varepsilon}}_i^2\right] \tag{14}$$

The estimator in (14) underestimates the variance values because the LS phase residuals are too small. Thus, other alternatives of the HCCM estimator in (14) were proposed in the literature (MacKinnon and White, 1985), and among them, a variation to better inflate the residuals and thus the variances obtained; the following estimator is, however, biased but it is considered less biased than the others (Hinkley, 1977; Efron, 1982; MacKinnon and White, 1985; Long and Ervin, 2000), and it is as follows

$$\mathbf{C}_{PhU_i} = diag\left[\frac{\widehat{\boldsymbol{\varepsilon}}_i^2}{(\mathbf{1} - \boldsymbol{h}_i)^2}\right] \tag{15}$$

where $\boldsymbol{h}_i$ is the vector of the principal diagonal elements of the following matrix $\mathbf{H}_i = \mathbf{B}_i\left(\mathbf{B}_i{}^T\mathbf{B}_i\right)^{-1}\mathbf{B}_i{}^T = \mathbf{B}_i\mathbf{B}_i^{\dagger}$. It has been shown experimentally that using one HCCM over another is driven by the number of available measurements, particularly by the number of used SAR interferograms. The work in (Long and Ervin, 2000) asserts that the estimator in (15) is more robust and should be used when measurements are below 250. Instead, when they are above 500, other HCCM estimators (MacKinnon and White, 1985), such as White's, see Eq. (14), can also be used, obtaining roughly very similar results. Because of the possible use of reduced subsets of interferograms, with cardinality even below 250, for the purposes of SAR interferometry, we recommend the general use of the estimator in (15). In addition, in the case of suspecting the heteroscedasticity condition of the error vector in (13), which is a condition for PhU errors, the solution of the OLS in (13) is unbiased but not at minimum error variance. Consequently, the solution to the linear problem loses its BLUE status. Moreover, to ensure the BLUE condition, generalized LS (GLS) solutions (Aitken, 1936) can be adopted by knowing the covariance matrices of interest, such as using the methods in (Akbari and Motagh, 2012; Hu et al., 2013; Falabella et al., 2020).

Finally, another source of uncertainties in the estimated ground displacement InSAR products is ascribed to the atmospheric stochastic fluctuations, which are modelled using the covariance matrix $\mathbf{C}_{turb\_APS_i}$. Both tropospheric and ionospheric layers cause a propagating delay in SAR echoes that affects the reliability of the estimated surface deformation terms (Hanssen, 2001; González and Fernández, 2011). The GB-SAR systems are not affected at all by any ionospheric disturbance, as only the lowest layer of the atmosphere is of interest, and thus atmospheric propagative phases are attributed only to the troposphere (Iglesias et al., 2014; Falabella et al., 2022a; Izumi et al., 2022a). In our scheme, the atmospheric covariance matrix $\mathbf{C}_{turb\_APS_i}$ considers exclusively the stochastic effects of the turbulent tropospheric structures present in each distribution of the analyzed SAR interferograms. In particular, the spatial dependence of the turbulent tropospheric delay, under the assumption of second-order intrinsic stationarity (Hanssen, 2001), can be quantified by employing a specific structure–function or variogram (Hanssen, 2001; Lohman and Simons, 2005) as follows

$$S(\Delta r) = E\left[\left(\Delta z(r) - \Delta z(r + \Delta r)\right)^2\right] \tag{16}$$

where $E[\cdot]$ is the statistical expectation operator, r is the spatial reference location, Δr is the spatial distance between the reference and other observation points, and $\Delta z(\cdot)$ represents the InSAR atmospheric turbulent function at given spatial locations. It can be shown that the turbulent atmospheric covariance matrix of SAR images, i.e., $\mathbf{C}_{turbulent}^{\mathrm{SAR}} \in \mathbb{R}^{N\times N}$ with N the number of acquired SAR scenes (Emardson et al., 2003; González and Fernández, 2011), is diagonal. The elements of this matrix can be estimated by following a network-based variance–covariance estimation (NVCE) method (Cao et al., 2018), which allows obtaining more reliable covariance values by focusing only on coherent SB SAR interferograms or even by using other valid approaches (González and Fernández, 2011; Kirui et al., 2022).

Therefore, using the errors propagation law (Ku, 1966) and considering the i-*th* SAR dataset, the atmospheric covariance matrix $\mathbf{C}_{turb\_APS_i}$ of the i-*th* InSAR distribution can be easily obtained as

$$\mathbf{C}_{turb\_APS_i} = \mathbf{B}_i \bullet \mathbf{C}_{turbulent}^{\mathrm{SAR}^{(i)}} \bullet \mathbf{B}_i^T \tag{17}$$

where $\mathbf{B}_i$ is the design matrix of the i-*th* InSAR distribution.

3.3. 3-D ground displacements variance–covariance matrix

Once the covariance matrixes $\mathbf{C}_{n_i}$, $\mathbf{C}_{PhU_i}$, and $\mathbf{C}_{turb\_APS_i}$ are computed

for each LOS platform, the terms $\mathbf{C}_{g_i}$ (e.g., for $i = 1, 2, 3$) are estimated (see Eq. (3)) and finally combined under the errors propagation law (Birge, 1939; Ku, 1966) to obtain the following 3-D ground displacement time series (Up-Down, East-West, and North-South) covariance matrix:

$$\mathbf{C}_{3-\mathrm{D}} = \mathbf{A}_d^{\dagger} \bullet \mathbf{C}_{g_{multi-platform}} \bullet \mathbf{A}_d^{\dagger^T} \tag{18}$$

where $\mathbf{A}_d^{\dagger} \in \mathbb{R}^{3N_{SYNC} \times 3N_{SYNC}}$ is the pseudoinverse of the design matrix (see also Eq. (6)) and $\mathbf{C}_{g_{multi-platform}} = \begin{bmatrix} \mathbf{C}_{g_1} & \mathbf{0} & \mathbf{0} \\ \mathbf{0} & \mathbf{C}_{g_2} & \mathbf{0} \\ \mathbf{0} & \mathbf{0} & \mathbf{C}_{g_3} \end{bmatrix} \in \mathbb{R}^{3N_{SYNC} \times 3N_{SYNC}}$ is the sparse partitioned matrix composed of the covariance matrices obtained for each LOS platform and the zeros matrices.

4. Case-study area and available SAR data

The case-study area is in Gorgoglione town, in the southwestern part of Matera Province (Basilicata Region, southern Italy), in a hilly area at about 800 m a.s.l. (see Fig. 3).

The terrain outcropping in the area is chaotic slope debris and alluvial deposits resting on the Gorgoglione Flysch Formation. This latter is a thick succession of alternating silty-marly clays and sandstones (Lentini et al., 2002; Cavalcante et al., 2015).

The lithological nature of the outcropping terrains and their structural setting determine the geomorphological aspects of the area. Due to the different erodibility degrees of the terrains, the landscape is undulating, characterized by narrow and sometimes deep incisions and intense erosive processes. The steepest and highest slopes identify the areas where most weathering-resistant lithotypes outcrop, while the morphologically more depressed zones correspond to the outcrop areas of softer formations.

According to the Italian Plan for the Hydrogeological Risk Protection (PAI, https://www.adb.basilicata.it/adb/pStralcio/piano2021vigente.asp), the investigated slope is classified as high landslide hazard zone – R3 (see Fig. 3) and has been affected by widespread instability phenomena linked to the presence of an ancient landslide body composed of a chaotic detrital material (coarse blocks immersed in a finer matrix). This landslide, active since 1980, is a complex movement showing rotational and translational components. Within the main body, secondary movements are recognized due to the differential settlement phenomena of the stone blocks immersed in the clayey matrix.

The change of soil moisture conditions in the subsoil due to the infiltration of rainwater and leakage from obsolete white and potable water networks, together with the growing urbanization of the area, can be considered the leading causes of the reactivations on the slope.

The reactivations, which have taken place over the years, have caused a continuous lowering of the Zanardelli Square (up to 20 cm), damages to the structures and infrastructures and the eviction of many

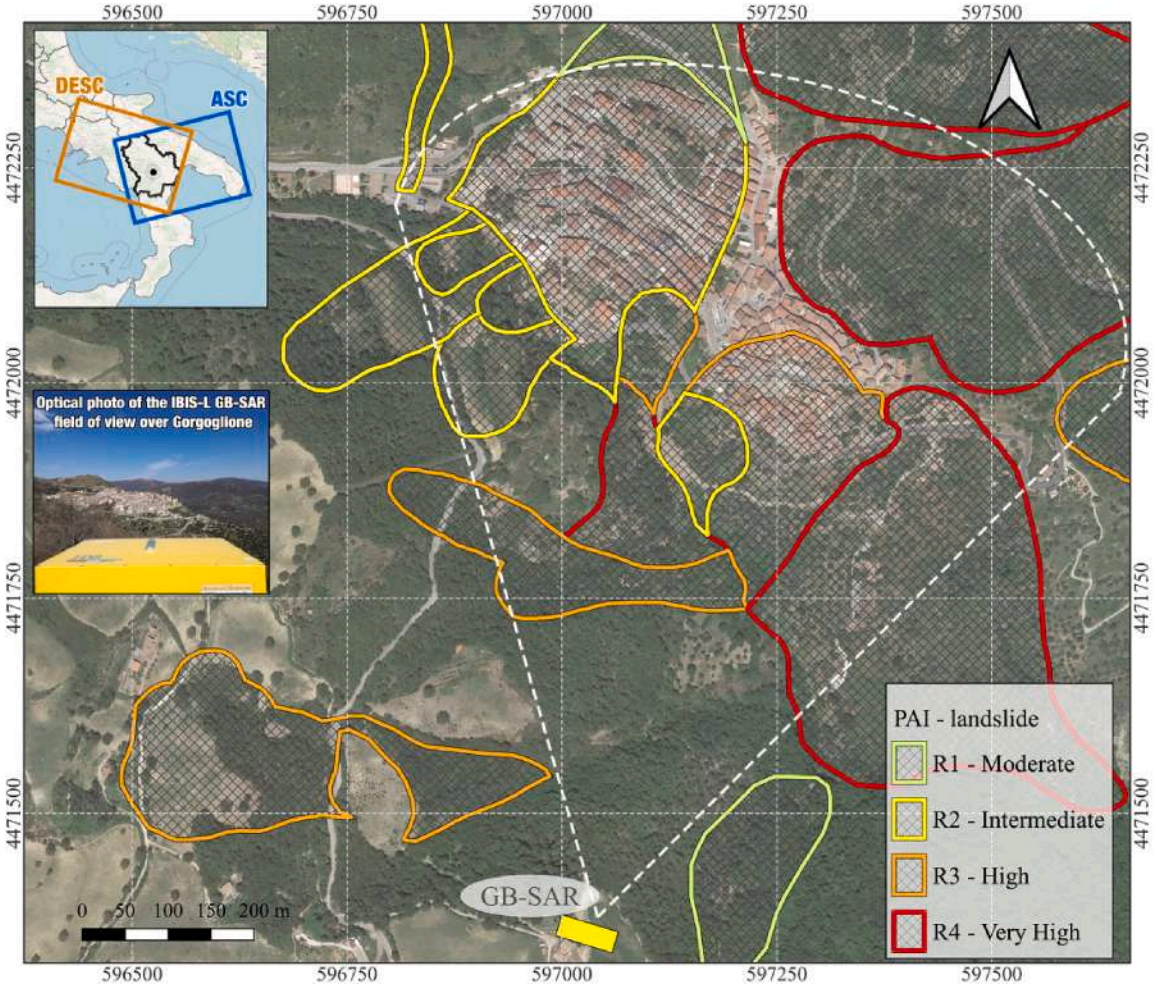

Fig. 3. Location map of Gorgoglione town in Basilicata Region (southern Italy) and position of the GB-SAR sensor (the white dashed polygon shows the sensor footprint). The upper left panel shows the ascending (Path 146) and descending (Path 124) Sentinel-1 footprint, blue and orange, respectively. The panel on the middle left shows an optical photo of the field of view of the GB-SAR IBIS-L; the average monitoring range between the GB-SAR and the center of the investigated area is about 800 m. The four landslide hazard zones R1-R4, as defined by PAI, are also reported. [The figure has been produced using QGIS open-source software]. (For interpretation of the references to color in this figure legend, the reader is referred to the web version of this article.)

houses.

Considering this, over the years, the local and national administrations have monitored the area to correctly plan intervention works for the safety of the whole slope.

The investigation period of our analysis is between September 2016 and July 2017, for which ascending and descending satellite SAR images and GB-SAR acquisitions are jointly available. Sentinel-1 (S-1) A/B (C-Band) ascending (Path 146) and descending (Path 124) orbit acquisitions have been used for the satellite side, while for the terrestrial platform has been employed an independent stack of IBIS-L (Bozzano et al., 2010; Cai et al., 2021) GB-SAR (Ku-Band) images. The field of view of IBIS-L on the Gorgoglione test case can be seen through an optical image in Fig. 3. Twenty-four (quasi-synchronous) time-epochs were identified by considering the three independent SAR datasets available and following the SAR image selection procedure in Section 2.2. Vertical-to-vertical (VV) polarization was employed for the interferometric purpose, and no one constraint was imposed for the geometrical perpendicular baseline. In contrast, for limiting temporal decorrelation, a maximum temporal baseline of 96 days was adopted for both platforms. Notably, the GB-SAR operated in zero perpendicular baseline configuration (avoiding any decorrelation due to geometrical antenna differences) without squinting the antennas, and it was installed on a promontory in front of the most vulnerable investigated area, i.e., the area near Zanardelli Square, which is the area most affected by the landslide. Furthermore, the centre-beam GB-SAR LOS forming an angle of 24° to the North direction provides excellent sensitivity to discern the N-S movement of the landslide (see Fig. 3).

5. Experimental results

5.1. LOS-projected ground displacement maps

This subsection shows the mean velocity LOS displacement maps obtained for satellite (ascending and descending orbits) and terrestrial (GB-SAR) platforms, also highlighting the critical steps adopted to achieve the showed InSAR products.

First, focusing on satellite processing, the wrapped co-registered (single-look) interferograms were adequately compensated for topographic and orbital components, respectively, using one-arcsec shuttle radar topography mission (SRTM) digital elevation model (DEM) of the scene and precise orbits of the Sentinel-1 A/B satellites. Then, the Mt-InSAR multigrid technique proposed by (Falabella et al., 2022b) was applied to obtain the InSAR products at full spatial resolution (the single-look Sentinel-1 A/B spatial resolution). Following the mathematical core of the adopted multigrid method (Falabella et al., 2022b), among the selected stable pixels, only those with a temporal coherence greater than or equal to 0.6 were considered well-processed pixels; this task allows the selection of stable pixels at full resolution and the exclusion of those strongly affected by PhU errors from this selection. A final stage of spatial low-pass (LP) and temporal high-pass (HP) filtering was applied directly to the estimated LOS ground displacement time series to mitigate turbulent atmospheric artefacts (Ferretti et al., 2001; Berardino et al., 2002).

Moving to the GB-SAR side, the generated wrapped single-look interferograms were flattened by removing the tropospheric phase screen using the Wrapped SPectral analysis for the APS compensation (WSP-APS) methodology (Falabella et al., 2022a), but other methods can also be adopted (Iglesias et al., 2014; Qiu et al., 2016; Chao et al., 2019). Subsequently, the flattened interferograms were independently unwrapped via the minimum cost flow (MCF) solver (Costantini, 1998). Note that the removal of tropospheric APS is performed directly on wrapped data via the WSP-APS algorithm, which makes the subsequent mandatory PhU procedures much more straightforward. In addition, the adopted APS compensation strategy can also track and remove the tropospheric screen fluctuation closely related to the changing orthometric height of the imaged scene, not needing any DEM of the scene. Thus, the InSAR ground displacement products are retrieved by OLS minimization using the unwrapped interferograms, as done, for example, in (Berardino et al., 2002). We point out that also for the GB-SAR LOS analysis, well-processed stable pixels at full resolution were identified using the same reliability estimators used for the satellite counterpart, described in detail in (Falabella et al., 2022b), and in particular by setting a threshold of 0.95 for the temporal coherence value. We remark that the adopted thresholds for both satellite and terrestrial estimators' values are experimentally chosen and, for each platform, they depend on the number of decorrelation sources, SAR scenes, interferograms and other parameters, so different estimation thresholds are adopted; for an in-depth lecture on the subject, see (Pepe, 2021) and references therein.

Finally, for both platforms, the well-processed pixels were georeferenced, and a simple nearest-neighbour (NN) procedure was performed to identify common pixels in the three datasets. Alternatively, instead of simple NN, if more accurate DEMs are available, more accurate georeferencing methods can be adopted, such as the method proposed in (Wang et al., 2022). The georeferenced LOS mean displacement velocity maps, superimposed to an optical image of the small Gorgoglione town via Google Earth engine, are shown in Fig. 4. The town is almost stable except for a small area located in the south of Gorgoglione, where, in the other hand, deformation due to the slow landslide that afflicts the town is visible. These negative deformation values are measured as a moving away from the sensor. They are recorded by both satellite sensors for ascending and descending orbit, respectively, in Fig. 4 (a) and (b). Similarly, the IBIS-L sensor records an appreciable deformation field for the same deforming area, shown in Fig. 4 (c), but in this case, the positive deformation values are measured as approaching the GB-SAR sensor. To evidence the direction in which deformation occurs, for each SAR platform, the LOS direction is indicated as a white-coloured arrow in Fig. 4. In terms of magnitude, maximum LOS mean displacement values of 15 mm/year were recorded during the investigation period.

5.2. 3-D ground displacement maps

The 3-D ground displacement velocity maps are retrieved over the group of common geocoded well-processed pixels already identified in the previous subsection, which are the georeferenced pixels for which the three independent LOS measures are available. To pass from the LOS measures to the Up-Down, East-West, and North-South ones, the mathematical rationale presented in Section 2.1 was applied. Local incidence angles range from 45.04° to 45.07° and from 33.33° to 35.64° for the ascending and descending orbit of Sentinel-1 A/B sensors, respectively. At the same time, 9.02° and 10.46° are the average heading angles for the ascending and descending tracks, respectively. For the IBIS-L sensor, however, the local incidence angles range from 76.20° to 90.30° with heading angles from 24.5° to 91°. Fig. 1 provides a pictorial representation of a 3-D geometry identifying local incidence and heading angles.

Fig. 5 shows the geocoded 3-D mean displacement velocity maps, where notable U-D and N-S displacements are evident by analyzing Fig. 5 (a) and (c). Whereas, no considerable deformation is appreciated in the E-W direction [see Fig. 5 (b)].

Therefore, the area affected by the landslide is prone to ground deformations in a southerly and downward direction, in accordance with the geomorphological characteristics of the landslide itself.

To better interpret the three-dimensional movement of the landslide, the vectorial representation of the geocoded 3-D mean displacement velocity has been mapped in Fig. 6. The map highlights the different dynamics affecting the urban center of Gorgoglione. According to the landslide map of the regional PAI, the areas classified as R2-Intermediate risk (delimited by yellow lines in Fig. 6) are characterized by a vertical ground velocity between −2.5 and 2.5 mm/y, so they can be considered stable.

The areas classified as R3-high risk (delimited by orange lines in Fig. 6) show a vertical ground velocity from −2.50 to −12.50 mm/y. The

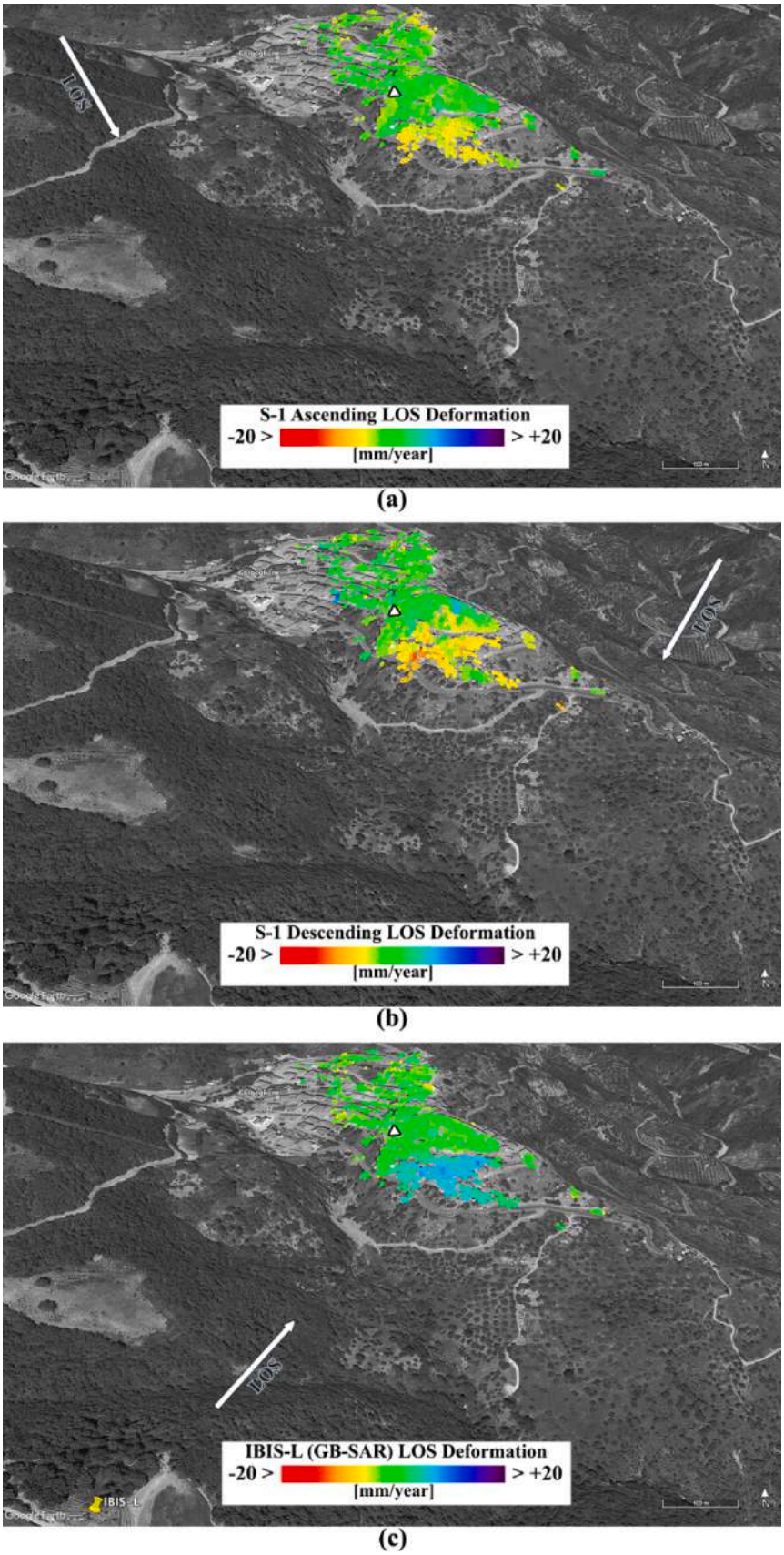

Fig. 4. Geocoded LOS mean displacement velocity maps. (a) Sentinel-1 ascending track. (b) Sentinel-1 descending track. (c) IBIS-L GB-SAR: The yellow-coloured dot marker identifies the position of the sensor. The white triangle identifies the location of the spatial reference point. Only stable pixels in the common overlap between GB-SAR and the satellite (ascending and descending) are shown. (For interpretation of the references to color in this figure legend, the reader is referred to the web version of this article.)

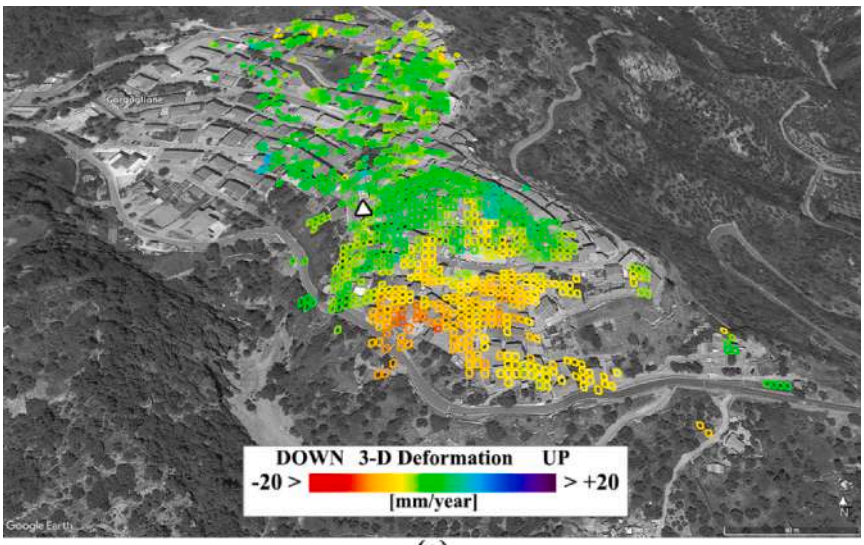

(a)

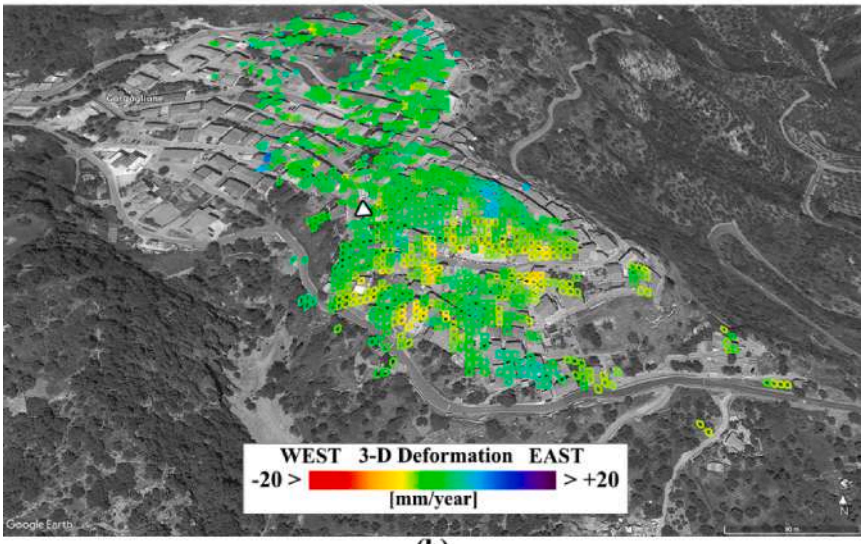

(b)

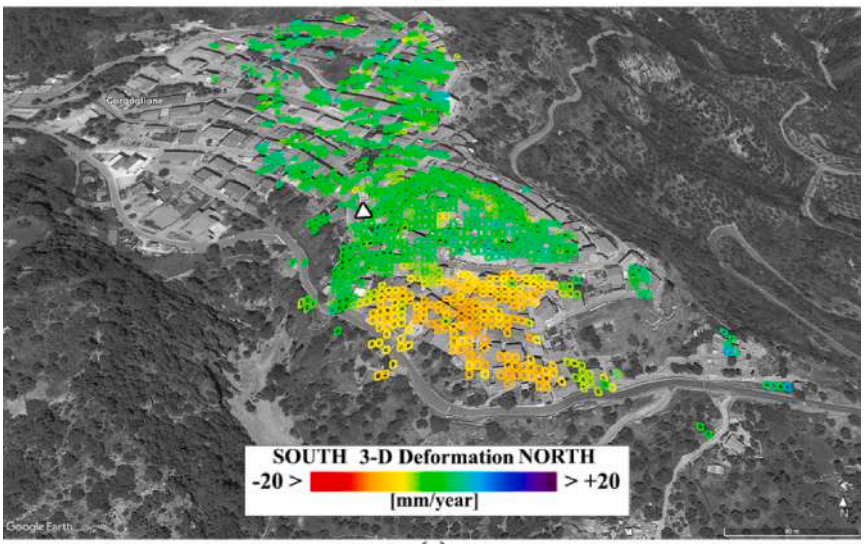

(c)

Fig. 5. Geocoded 3-D mean displacement velocity maps. (a) Up-Down. (b) East-West. (c) North-South. The white triangle identifies the location of the spatial reference point. Only stable pixels in the common overlap between GB-SAR and the satellite (ascending and descending) are shown.

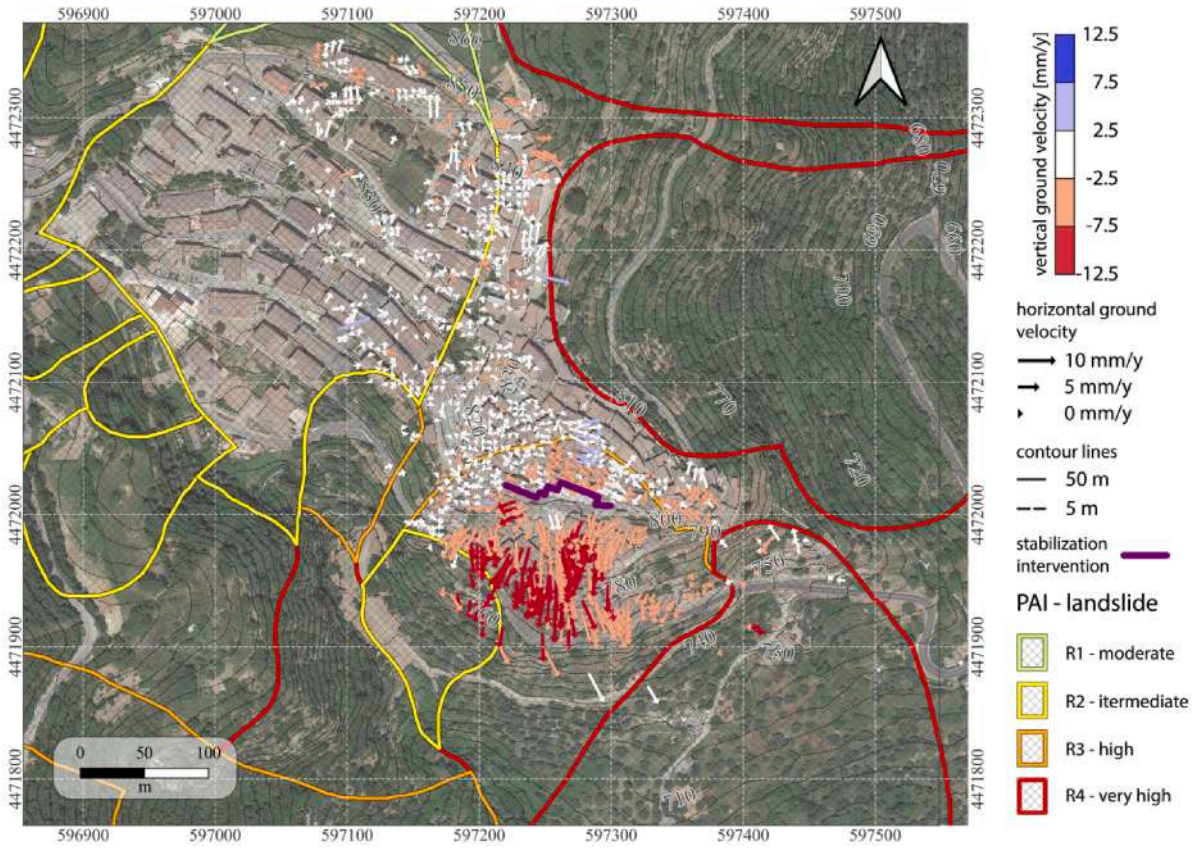

Fig. 6. Vectorial representation of the geocoded 3-D mean displacement velocity. Arrow intensity represents the horizontal ground velocity, while the arrow color indicates the vertical component of the ground velocity. The solid violet polyline denotes the stabilization intervention carried out on the north side of Zanardelli Square at the end of the 90 s. The four landslide hazard zones R1-R4, as defined by PAI, are again reported. (For interpretation of the references to color in this figure legend, the reader is referred to the web version of this article.)

highest values > -7.50 mm/year are more evident in the portion of the slope located south of Zanardelli Square.

According to the technical documents provided by the local administration of the Gorgoglione municipality, since 1980, this portion of the historic centre has been affected by a landslide, which, over the years, has undergone various reactivations. The most important occurred in May 2004 and December 2013, causing a continuous lowering (up to 20 cm) of the Zanardelli Square, damage to homes and infrastructures, and the eviction of some houses.

A first stabilization intervention, consisting of a retaining wall built on poles and with tie rods at different heights, was carried out by the regional administration on the north side of Zanardelli Square at the end of the 90 s (solid violet polyline in Fig. 6). After the 2004 and 2013 events, the national administrations mainly studied and monitored the area (Civil Protection and Government). Funds were allocated for building stabilization works, consisting of bulkheads and micro piles. The outcomes for these interventions began in 2019, after our observation period.

The retaining wall built at the end of the 90 s is highlighted in Fig. 6; indeed, precisely at the northern limit of Zanardelli Square, there is a consistent variation in the direction of the arrows to what is observed south of Zanardelli Square. They show an almost east–west movement that seems to follow the course of the retaining wall in parallel with a displacement velocity of less than 3 mm/y.

On the contrary, a movement in the opposite direction, from north to south and of greater intensity (horizontal ground velocity up to 10 mm/y and vertical ground velocity up to 12–13 mm/y, see Fig. 6), characterizes the portion of the slope located in the southern part of Zanardelli Square.

The displacement trend shown in the 3D landslide vector map of Fig. 6 highlights the correct operation of the retaining wall that proves to contain the movement of the slope north of Zanardelli Square. Nothing can be said about the effectiveness of the interventions carried out in 2019 as executed outside our observation period.

5.3. *Analysis of the 3-D ground displacement products uncertainties*

In this subsection, the statistical framework for quality assessment of the 3-D ground displacement time series, developed in Section 3, is applied by exploiting the three available quasi-synchronous SAR dataset of Gorgoglione town, independently gathered from the S-1 A/B sensors (ascending and descending orbits) and the IBIS-L GB-SAR sensor. For each geocoded pixel common to the three datasets, the 3-D covariance matrix was computed following the formalism in Subsection 3.3. We point out that only uncertainties due to decorrelation terms and time-inconsistent PhU errors were considered for this specific case study. This choice is dictated by the fact the area only extends for about 400x400 meters, where uncertainties due to stochastic atmospheric turbulent structures can be neglected without affecting the obtainable three-dimensional covariance matrices. More precisely, since the atmospheric uncertainties are modelled as strictly increasing monotonic functions (i.e., the structure functions), dependent on the spatial distances between a spatial reference point and others, these additional uncertainty terms can be neglected as the analyzed scene is small. Thus, we modelled the uncertainty terms for each platform dataset by applying the methods in Subsection 3.1 and 3.2, respectively, for decorrelation phenomena and PhU errors. Therefore, the 3-D partitioned covariance matrices [see Eq. (18)] are obtained for each well-processed pixel in the scene. The elements on the main diagonal of these partitioned matrices are the variances of each quasi-synchronous measurement for the E-W, U-D and N-S ground displacement time

series. To obtain synthetic reliability indicators for each 3-D direction, i.e., for the E-W, U-D, and N-S time series, we properly extracted and averaged the elements on the main diagonal of the 3-D covariance matrices. The roots of these averaged values (mean standard deviation values) represent the error of each measure (each time-series sample) and, for each geocoded pixel, are shown in Fig. 7. Furthermore, spatially averaging these error values overall results in mean standard deviation values of 3.74 mm, 3.62 mm, and 0.66 mm, respectively, for the E-W [Fig. 7 (a)], U-D [Fig. 7 (b)], and N-S [Fig. 7 (c)] directions. In contrast, for the same 3-D directions, the maximum error bounds reach values of 5.02 mm (E-W), 4.69 mm (U-D) and 3.07 mm (N-S). The carried out E-W and U-D standard deviation values are in general accordance with other previous quality assessment investigations, e.g., with the work in (Casu et al., 2006); indeed, they are even smaller because of the contribution in terms of accuracy provided by the high-reliability GB-SAR measurements. Remarkably, very fine accuracies are achieved for the ground displacement time series obtained for the N-S direction. In this context, we selected four pixels of interest, namely P1, P2, P3, and P4, which can be identified in Fig. 7 (a) and for which the 3-D ground displacement time series (see Fig. 8) were also computed using the procedure fully detailed in subsection 2.2. Fig. 8 (a) shows subtle deformations for the P1 pixel along the U-D and E-W directions, which mostly fall within the standard deviation of the measurements themselves. In contrast, the deformation in the south direction is characterized by an average standard deviation of 0.76 mm, so it is highly reliable.

Similarly, the downward and southward deformations of pixel P2 [see Fig. 8 (b)] do not fall within the error values obtained for the two directions, respectively, 3.07 mm (U-D) and 0.62 mm (N-S). Pixels P3 and P4, shown in Fig. 8 (c) and (d) show noteworthy deformation only in the N-S direction and specifically southward. P3 is subjected to a maximum deformation of 9 mm (in moduli) along the south at the end of the investigation period. At the same time, it is noteworthy that the nonlinear deformation along the N-S direction to which pixel P4 is subjected, given the standard deviation value of 0.60 mm, is considered plausible and reliable. Ultimately, all four selected pixels are subject to deformation to be deemed reliable along the N-S direction and predominantly toward the south direction, confirming the slow downward and southward landslide-induced movement to which the deforming zone of Gorgoglione town is subject.

Unfortunately, external data for validation (such as GPS, inclinometer measurements, etc.) are not available in the analyzed area. As stated in Section 4, the site is subjected to a very slow-moving landslide that has been active since 1980, responsible for several cracks and effects observed on the main roads of the historic center. Local authorities, which simply monitor the landslide effects on the built environment, confirmed that the cracks' magnitude is a few millimeters. This is qualitatively consistent with our results, but it is insufficient to provide readers with a quantitative analysis of the evaluated uncertainties of 3-D displacements. However, due to the free availability of LOS InSAR ground displacement time series derived from Sentinel-1 A/B sensors and provided by the European Ground Motion Service (EGMS) (https://egms.land.copernicus.eu), a straightforward cross-comparison analysis was conducted between our products and those available at EGMS. Specifically, we have first selected the ascending and descending EGMS L2b LOS ground displacement time series (same paths as our datasets). Then, we performed a georeferencing procedure between the two orbits and then between the 3D InSAR products achieved with our method. From the set of well-georeferenced pixels, we have combined the two EGMS L2b orbits to discriminate the U-D and E-W components (the N-S direction is essentially blind), and subsequently, we compared these latter components with the ones obtained by applying our methodology. It is worth emphasizing that the combination method discussed in our work can detect and follow the N-S ground deformations profile, but for comparison consistency, we only show the U-D and E-W profiles of four pixels of interest. The selected pixels are labelled as Q1, Q2, Q3 and Q4, and their markers can be seen in Fig. 7 (b). We point out that the selected points (Q1, Q2, Q3 and Q4) are located near the position of points (P1, P2, P3, and P4) shown in Fig. 8. We selected a different set of points to do the comparison analysis due to the lack of coherent and well-processed points on the same scatterers on the ground for ascending and descending EGMS L2b products. Note also that the EGMS products over the Gorgoglione area were spatially sparser and with a coarser resolution than those presented in our work. Fig. 9 compares the ground deformation time series of the four points of interest, calculated by the Copernicus EGMS service (asterisks) and through our framework (triangles). The U-D and E-W ground displacement time series show a general agreement between the products. Moreover, the tiny differences are even below the theoretical error bounds estimated from our developed statistical error framework. We would like to remark that as good as comparisons can be, we are dwelling on the differences in processing between the methods used by EGMS and us; however, the source data are basically the same, and what is presented here is only a result of a cross-comparison analysis. Nevertheless, the EGMS products are generally validated through geodetic networks; thus, the good agreement between the products obtained by our method and those of EGMS can be seen as a confirmation of the effectiveness and robustness of the proposed method, even though it cannot be seen as an external validation of the proposed statistical framework. Its quantitative assessment would require processing several independent sets of SAR data collected by satellite and terrestrial systems in heterogeneous ground deformation conditions: This is far beyond the limits of the present work, and it is a matter for future investigations conducted by independent scholars.

Furthermore, a simulation was carried out to give evidence of the improvement achieved in the accurate discrimination of the N-S profile in the 3-D space when an appropriately positioned GB-SAR sensor is integrated with the satellite sensors. To this end, we considered the actual multi-platform configuration of the Gorgoglione case, consisting of acquisitions collected from two Sentinel-1 orbits (ascending and descending) and one GB-SAR campaign from IBIS-L. Specifically, we simulated a N-S deformation pattern that ranges from 0 to 40 mm with a step size of 0.25 mm, and we evaluated the line-of-sight projections of this signal to the Sentinel-1 and GB-SAR illumination geometries. This simulation helps demonstrate that, properly mounted on the ground, a GB-SAR system can discern the N-S component with improved precisions to quasi-polar satellite systems like Sentinel-1. Fig. 10 shows graphs that demonstrate the estimated LOS-projected ground deformation values for the satellite systems (blue triangles) are within the LOS measurement error bars (as computed considering the actual system configuration), whereas the LOS values for the GB-SAR system (red points) greatly exceed the estimated GB-SAR LOS precisions; 5 mm and 0.3 mm, for the satellite and GB-SAR sensors, respectively. Note that the computed GB-SAR LOS error bound is 0.3 mm, and it is consistent also with the precision values indicated in the IBIS-L GB-SAR datasheet and also reported by other scholars (Rödelsperger et al., 2010; Qiu et al., 2016; Wang et al., 2020).

6. Discussion

The results obtained for the Gorgoglione slow-varying landslide case study proved the usefulness of the proposed combined approach in studying the 3-D differential landslide movements. The revealed 3-D ground displacement components allowed us to highlight the investigated phenomenon's complexity and evaluate the stability and functionality of the retaining wall built to contain the movement of the Northern slope of Zanardelli Square. As stated in Section 4, the studied landslide is a complex movement showing rotational and translational components and secondary movements due to the differential settlement phenomena of the stone blocks embedded in the clayey matrix. The different types of movement and the lithological heterogeneity of the outcropping terrains inevitably cause significant changes in ground deformation rates observed along the different LOS directions. The analysis of the P1-P4 time series highlights this behaviour. Conversely,

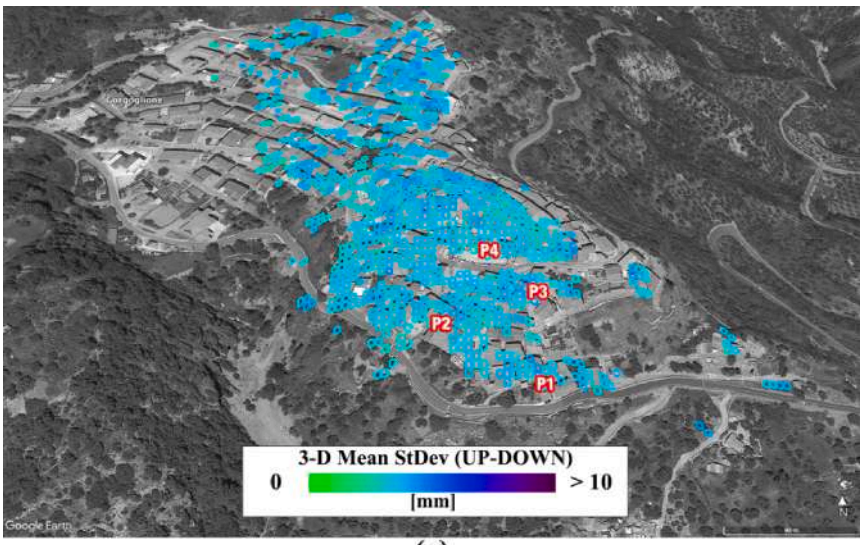

(a)

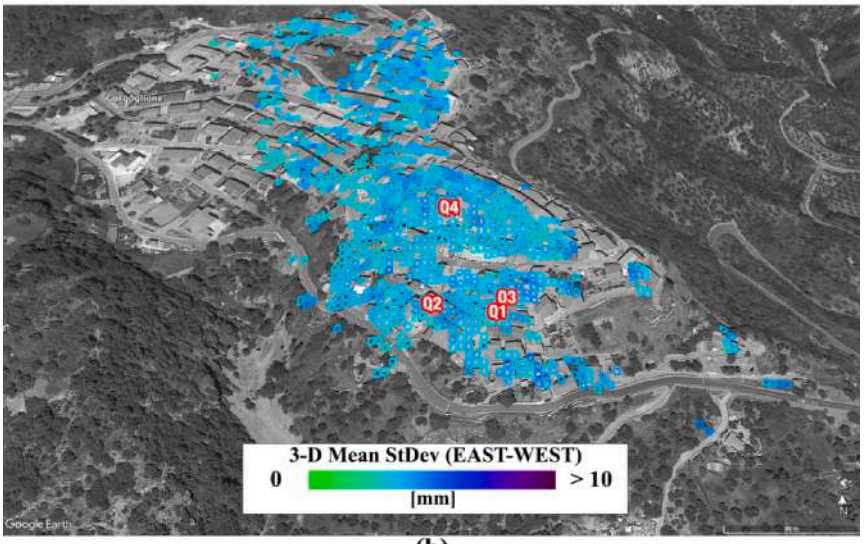

(b)

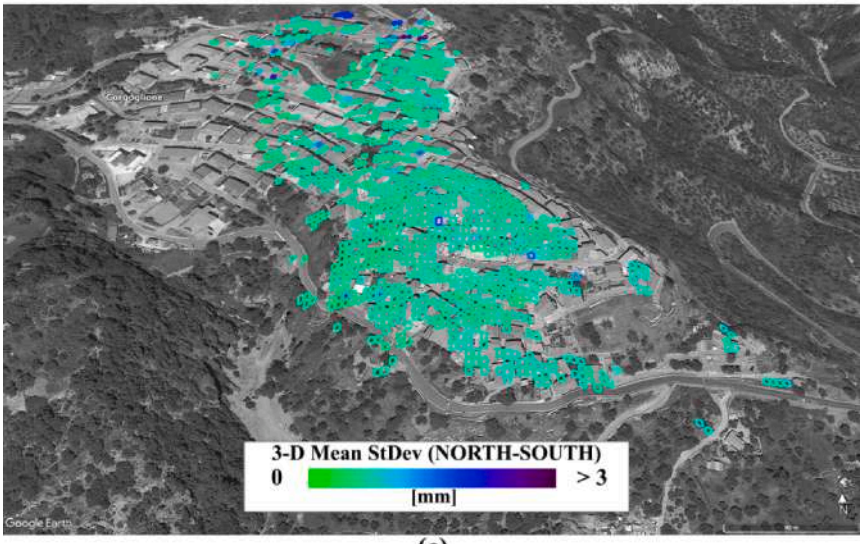

(c)

Fig. 7. Geocoded 3-D mean standard deviation maps related to the accuracy of single measurements in the 3-D ground displacement time series. (a) Up-Down. (b) East-West. (c) North-South. Also identifiable in (a) and (b) are eight pixels of interest labelled P1, P2, P3, P4, Q1, Q2, Q3, and Q4. Only stable pixels in the common overlap between GB-SAR and the satellite (ascending and descending) are shown.

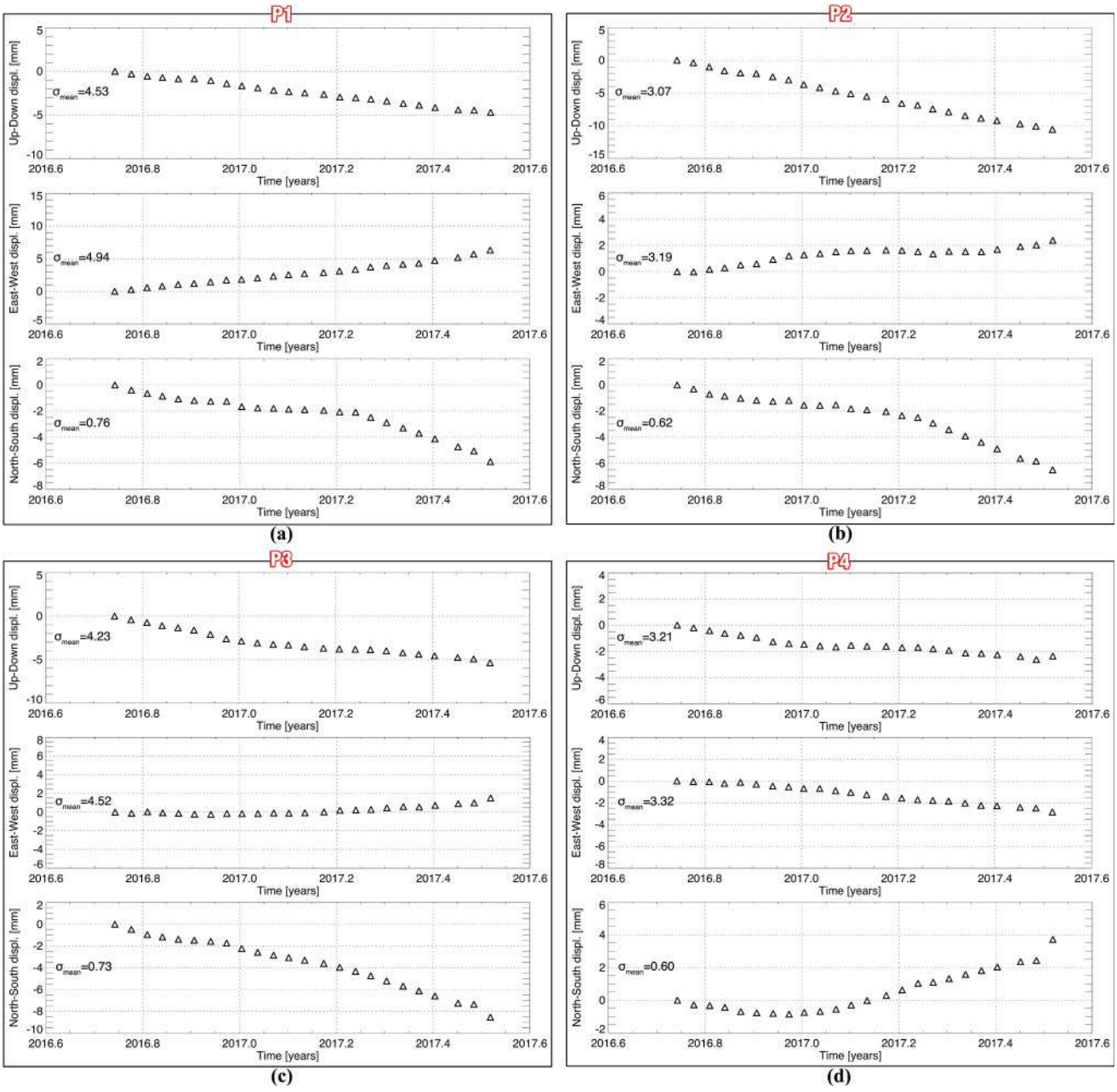

Fig. 8. 3-D ground displacement time series for the four pixels of interest, also identified in Fig. 7 (a), namely P1 (a), P2 (b), P3 (c), and P4 (d). The U-D, E-W and N-S, ground displacement time series, are shown with their mean standard deviation values for each selected pixel, grouping the three components into black continuous line boxes.

P1 and P2 points are in the landslide accumulation zone; after March 2017, they showed an apparent acceleration of the deformation, unlike point P3, which is positioned close to the lateral boundary of the landslide.

Furthermore, the analysis of the precipitations collected by the Gorgoglione rain gauge station (available at the Basilicata Region Functional Center website - https://www.centrofunzionalebasilicata.it/it/) highlights the occurrence of a period of continuous rain throughout January and early February 2017. The hypothesis that might explain the observed ground displacements is that the rainwater infiltration may have increased the pore pressures within the soil, thus causing an acceleration in the translational movement (Fig. 8a and b) of the terrigenous component that characterizes the areas where P1 and P2 are located. Moreover, P3 is characterized by a constant deformation trend without any evident acceleration; it could be found on a more resistant lithotype that has not been affected by the increase of pore pressures.

The results also highlighted the correct operation of the retaining wall built at the end of the 90 s. Indeed, the wall seemed to effectively contain the material placed upstream, constituting an obstacle to the possible retrogression of the landslide crown towards the upper part of the inhabited center. Nevertheless, a more careful analysis of the P4 time series (located on the wall) showed a particular deformation pattern along the North-South direction, with a first small southward deformation followed by a northward deformation after February 2017. The analysis of time series related to other points located on the wall confirmed similar patterns, leading to hypothesize that the rainfall has also accelerated the rotational component of the phenomenon, causing a rotation at the base of the retaining wall, which results in a northward movement at the top of the wall.

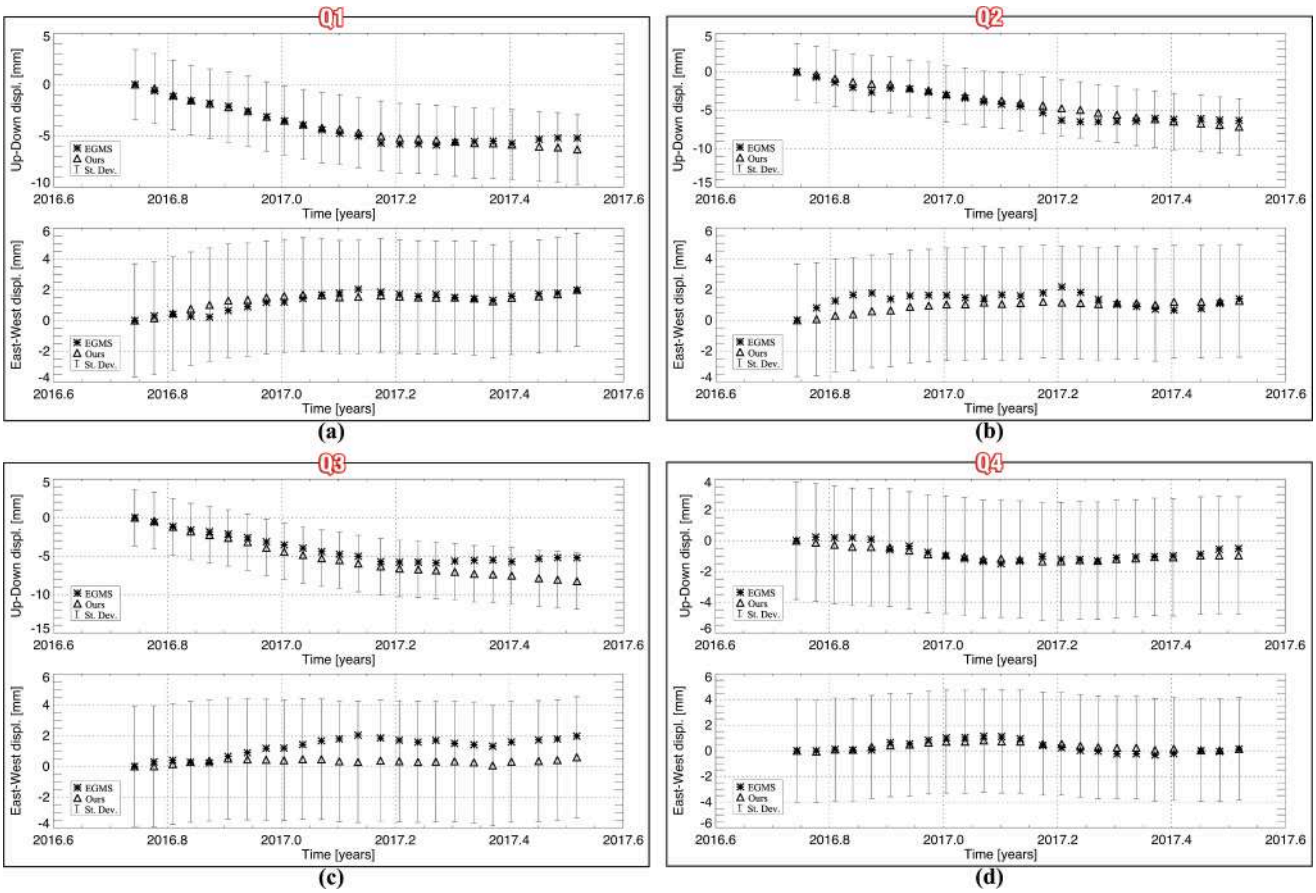

Fig. 9. Comparison between 2-D ground displacement time series obtained from EGMS L2b products and ours for the four pixels of interest, also identified in Fig. 7 (b), namely Q1 (a), Q2 (b), Q3 (c), and Q4 (d). The U-D and E-W, ground displacement time series, are shown with their mean standard deviation values for each selected pixel, grouping the two components into black continuous line boxes.

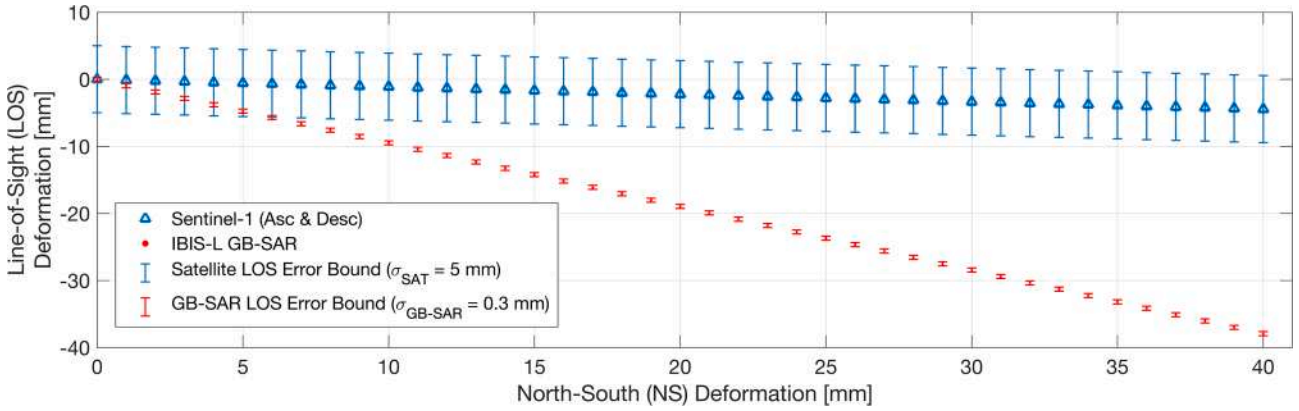

Fig. 10. Simulation of an N-S profile and evaluation of its impact on the lines of sight of a GB-SAR sensor (suitably positioned) and satellite (ascending and descending) quasi-polar sensors. The angles used for the simulation are the same as the real InSAR 3-D scenario, thus including Sentinel-1 (ascending and descending) and an IBIS-L GB-SAR sensor. The LOS error limits for both the satellite (5 mm) and GB-SAR (0.3 mm) cases were calculated using the developed statistical framework and are represented by the bars in red and blue for GB-SAR and satellite, respectively. (For interpretation of the references to color in this figure legend, the reader is referred to the web version of this article.)

7. Conclusion and further remarks

The main findings of our research are related to the systematic analysis of the quality of three-dimensional ground deformation time series obtained through differential interferometric synthetic aperture radar (InSAR) approaches, jointly applied to satellite and ground-based SAR observations. With experiments and theory analyses, we have demonstrated that the flexibility of the GB-SAR instrument positioning allows detecting with millimetric precisions the ground displacement occurring along the North-South direction, circumventing the problem of quasi-polar satellite orbits that lead to line-of-sight deformation measurements that are less sensitive to ground displacements occurring along North-South. From the statistical point of view, the general expression of the variance–covariance matrix of the obtained 3-D

ground displacement time series has been derived, considering the inherent statistical properties of the used interferograms, considering the noise artefacts (including the effects of decorrelation noise, time-inconsistent phase unwrapping errors and atmospheric phase disturbances). The adopted statistical framework can straightforwardly be extended to determine the precision of 3-D ground displacement InSAR products generated using several (more than three) complementary SAR datasets, also including the possibility of having two or more GB-SAR instruments installed on the ground and sets of SAR data acquired in distinctive epochs, by extending the presented statistical framework to the group of multi-satellite combination techniques recently developed in the literature (Wright et al., 2004; Samsonov and d'Oreye, 2012; Pepe et al., 2016). Furthermore, additional efforts are still required to fully characterize the phase unwrapping errors and APS disturbances referring to different ground displacement scenarios (due to heterogeneous causes, such as landslides, earthquakes, volcano eruptions, etc.) exploiting several independent SAR datasets.

Our work is propaedeutically for subsequent investigations to evaluate the quality of 3-D ground displacement products with present-day and forthcoming available archives of terrestrial, airborne, and spaceborne SAR images, with enhanced frequency repetition observations and complementary imaging views. Unfortunately, external independent measurements on the ground displacement were lacking for the Gorgoglione site. As earlier said, the quantitative assessment of the proposed statistical framework would require its application in several heterogeneous contexts where satellite and terrestrial SAR data are available. Also, the availability of detailed in situ geophysical, geological and geomorphological surveys would be needed to characterize the geophysical phenomena and the man-induced processes responsible for the observed ground displacement. This is a matter for future extensive investigations.

CRediT authorship contribution statement

Francesco Falabella: Conceptualization, Methodology, Software, Formal analysis, Writing – original draft preparation, Writing – review & editing, Visualization. **Antonio Pepe:** Conceptualization, Methodology, Formal analysis, Writing – review & editing. **Angela Perrone:** Conceptualization, Data curation, Writing – review & editing, Geological and geomorphological interpretation, Supervision. **Tony Alfredo Stabile:** Conceptualization, Data curation, Writing – review & editing, Visualization, Funding acquisition.

Declaration of competing interest

The authors declare that they have no known competing financial interests or personal relationships that could have appeared to influence the work reported in this paper.

Acknowledgement

The authors would like to thank the technical office of Gorgoglione municipality for providing us with geological and geotechnical documentation. A special thanks goes to N. Tragni, who helped generate some figures using QGIS open-source code. The authors acknowledge financial support under the National Recovery and Resilience Plan (NRRP), Mission 4, Component 2, Investment 1.1, program PRIN 2022, Decree No. 104 published on 2/2/2022 by the Italian Ministry of University and Research (MUR), funded by the European Union - NextGenerationEU - Project "Multiscale study of seismogenic processes in Campania-Lucania Apennines using machine learning algorithms and multiparametric observations (FRACTURES)" - CUP B53D23006980006 - Grant Number 2022BEKFN2.

References

Agram, P.S., Simons, M., 2015. A noise model for InSAR time series. J. Geophys. Res. Solid Earth 120, 2752–2771. https://doi.org/10.1002/2014JB011271.
Aitken, A.C., 1936. IV.—On least Squares and Linear combination of observations. Proc. r. Soc. Edinb. 55, 42–48. https://doi.org/10.1017/S0370164600014346.
Akbari, V., Motagh, M., 2012. Improved ground subsidence monitoring using small baseline SAR interferograms and a weighted least Squares inversion algorithm. IEEE Geosci. Remote Sens. Lett. 9, 437–441. https://doi.org/10.1109/LGRS.2011.2170952.
Ansari, H., De Zan, F., Bamler, R., 2018. Efficient phase estimation for interferogram stacks. IEEE Trans. Geosci. Remote Sens. 56, 4109–4125. https://doi.org/10.1109/TGRS.2018.2826045.
Ansari, H., De Zan, F., Parizzi, A., 2021. Study of systematic bias in measuring surface deformation with SAR interferometry. IEEE Trans. Geosci. Remote Sens. 59, 1285–1301. https://doi.org/10.1109/TGRS.2020.3003421.
Anscombe, F.J., Tukey, J.W., 1963. The examination and analysis of residuals. Technometrics 5, 141–160. https://doi.org/10.2307/1266059.
Bamler, R., Hartl, P., 1998. Synthetic aperture radar interferometry. Inverse Probl. 14, R1–R54. https://doi.org/10.1088/0266-5611/14/4/001.
Baran, I., Stewart, M., Claessens, S., 2005. A new functional model for determining minimum and maximum detectable deformation gradient resolved by satellite radar interferometry. IEEE Trans. Geosci. Remote Sens. 43, 675–682. https://doi.org/10.1109/TGRS.2004.843187.
Bardi, F., Frodella, W., Ciampalini, A., Bianchini, S., Del Ventisette, C., Gigli, G., Fanti, R., Moretti, S., Basile, G., Casagli, N., 2014. Integration between ground based and satellite SAR data in landslide mapping: the san fratello case study. Geomorphology 223, 45–60. https://doi.org/10.1016/j.geomorph.2014.06.025.
Bayer, B., Simoni, A., Schmidt, D., Bertello, L., 2017. Using advanced InSAR techniques to monitor landslide deformations induced by tunneling in the northern apennines. Italy. Eng. Geol. 226, 20–32. https://doi.org/10.1016/j.enggeo.2017.03.026.
Bechor, N.B.D., Zebker, H.A., 2006. Measuring two-dimensional movements using a single InSAR pair. Geophys. Res. Lett. 33 https://doi.org/10.1029/2006GL026883.
Bekaert, D.P.S., Hooper, A., Wright, T.J., 2015. A spatially variable power law tropospheric correction technique for InSAR data. J. Geophys. Res. Solid Earth 120, 1345–1356. https://doi.org/10.1002/2014JB011558.
Berardino, P., Fornaro, G., Lanari, R., Sansosti, E., 2002. A new algorithm for surface deformation monitoring based on small baseline differential SAR interferograms. IEEE Trans. Geosci. Remote Sens. 40, 2375–2383.
Berrino, G., Corrado, G., Luongo, G., Toro, B., 1984. Ground deformation and gravity changes accompanying the 1982 Pozzuoli uplift. Bull. Volcanol. 47, 187–200. https://doi.org/10.1007/BF01961548.
Birge, R.T., 1939. The propagation of errors. Am. J. Phys. 7, 351–357. https://doi.org/10.1119/1.1991484.
Boncio, P., Pizzi, A., Brozzetti, F., Pomposo, G., Lavecchia, G., Di Naccio, D., Ferrarini, F., 2010. Coseismic ground deformation of the 6 april 2009 l'Aquila earthquake (central Italy, Mw6.3). Geophys. Res. Lett. 37 https://doi.org/10.1029/2010GL042807.
Bozzano, F., Mazzanti, P., Prestininzi, A., Scarascia Mugnozza, G., 2010. Research and development of advanced technologies for landslide hazard analysis in Italy. Landslides 7, 381–385. https://doi.org/10.1007/s10346-010-0208-x.
Cai, J., Jia, H., Liu, G., Zhang, B., Liu, Q., Fu, Y., Wang, X., Zhang, R., 2021. An accurate geocoding method for GB-SAR images based on solution space Search and its application in landslide monitoring. Remote Sens. 13, 832. https://doi.org/10.3390/rs13050832.
Cao, Y., Li, Z., Wei, J., Hu, J., Duan, M., Feng, G., 2018. Stochastic modeling for time series InSAR: with emphasis on atmospheric effects. J. Geod. 92, 185–204. https://doi.org/10.1007/s00190-017-1055-5.
Carlà, T., Farina, P., Intrieri, E., Ketizmen, H., Casagli, N., 2018. Integration of ground-based radar and satellite InSAR data for the analysis of an unexpected slope failure in an open-pit mine. Eng. Geol. 235, 39–52. https://doi.org/10.1016/j.enggeo.2018.01.021.
Carlà, T., Tofani, V., Lombardi, L., Raspini, F., Bianchini, S., Bertolo, D., Thuegaz, P., Casagli, N., 2019. Combination of GNSS, satellite InSAR, and GBInSAR remote sensing monitoring to improve the understanding of a large landslide in high alpine environment. Geomorphology 335, 62–75. https://doi.org/10.1016/j.geomorph.2019.03.014.
Casu, F., Manzo, M., Lanari, R., 2006. A quantitative assessment of the SBAS algorithm performance for surface deformation retrieval from DInSAR data. Remote Sens. Environ. 102, 195–210. https://doi.org/10.1016/j.rse.2006.01.023.
Casu, F., Manconi, A., Pepe, A., Lanari, R., 2011. Deformation time-series generation in areas Characterized by Large displacement dynamics: the SAR amplitude pixel-offset SBAS technique. IEEE Trans. Geosci. Remote Sens. 49, 2752–2763. https://doi.org/10.1109/TGRS.2010.2104325.
Cavalcante, F., Prosser, G., Agosta, F., Belviso, C., Corrado, G., 2015. Post-depositional history of the miocene gorgoglione formation (southern apennines, Italy): inferences from mineralogical and structural analyses. Bull. Société Géologique Fr. 186, 243–256. https://doi.org/10.2113/gssgfbull.186.4-5.243.
Chao, B., Lai, T., Zhang, D., Huang, H., 2019. An Overview of Atmospheric Correction for GB-SAR, in: 2019 IEEE 19th International Conference on Communication Technology (ICCT). Presented at the 2019 IEEE 19th International Conference on Communication Technology (ICCT), IEEE, Xi'an, China, pp. 1062–1072. 10.1109/ICCT46805.2019.8947295.
Chen, B., Deng, K., Fan, H., Hao, M., 2013. Large-scale deformation monitoring in mining area by D-InSAR and 3D laser scanning technology integration. Int. J. Min. Sci. Technol. 23, 555–561. https://doi.org/10.1016/j.ijmst.2013.07.014.

Cigna, F., Tapete, D., 2021. Sentinel-1 big data processing with P-SBAS InSAR in the geohazards exploitation platform: an experiment on coastal land subsidence and landslides in Italy. Remote Sens. 13, 885. https://doi.org/10.3390/rs13050885.
Collett, D., Lewis, T., 1981. Discriminating between the von mises and wrapped normal distributions. Aust. J. Stat. 23, 73–79. https://doi.org/10.1111/j.1467-842X.1981.tb00763.x.
Corsini, A., Farina, P., Antonello, G., Barbieri, M., Casagli, N., Coren, F., Guerri, L., Ronchetti, F., Sterzai, P., Tarchi, D., 2006. Space-borne and ground-based SAR interferometry as tools for landslide hazard management in civil protection. Int. J. Remote Sens. 27, 2351–2369. https://doi.org/10.1080/01431160600554405.
Costantini, M., 1998. A novel phase unwrapping method based on network programming. IEEE Trans. Geosci. Remote Sens. 36, 813–821. https://doi.org/10.1109/36.673674.
Costantini, M., Malvarosa, F., Minati, F., 2012. A general formulation for redundant integration of finite differences and phase unwrapping on a Sparse multidimensional domain. IEEE Trans. Geosci. Remote Sens. 50, 758–768. https://doi.org/10.1109/TGRS.2011.2162630.
Daout, S., Doin, M.-P., Peltzer, G., Socquet, A., Lasserre, C., 2017. Large-scale InSAR monitoring of permafrost freeze-thaw cycles on the tibetan plateau. Geophys. Res. Lett. 44, 901–909. https://doi.org/10.1002/2016GL070781.
De Zan, F., Zonno, M., Lopez-Dekker, P., 2015. Phase inconsistencies and multiple scattering in SAR interferometry. IEEE Trans. Geosci. Remote Sens. 53, 6608–6616. https://doi.org/10.1109/TGRS.2015.2444431.
Di Traglia, F., De Luca, C., Manzo, M., Nolesini, T., Casagli, N., Lanari, R., Casu, F., 2021. Joint exploitation of space-borne and ground-based multitemporal InSAR measurements for volcano monitoring: the Stromboli volcano case study. Remote Sens. Environ. 260, 112441 https://doi.org/10.1016/j.rse.2021.112441.
Ding, J., Zhao, Q., Tang, M., Calò, F., Zamparelli, V., Falabella, F., Liu, M., Pepe, A., 2020. On the Characterization and forecasting of ground displacements of ocean-reclaimed lands. Remote Sens. 12, 2971. https://doi.org/10.3390/rs12182971.
Dobson, A.J., 1978. Simple approximations for the von mises concentration statistic. J. R Stat. Soc. Ser. C Appl. Stat. 27, 345–347. https://doi.org/10.2307/2347172.
Dong, J., Zhang, L., Tang, M., Liao, M., Xu, Q., Gong, J., Ao, M., 2018. Mapping landslide surface displacements with time series SAR interferometry by combining persistent and distributed scatterers: a case study of jiaju landslide in danba China. Remote Sens. Environ. 205, 180–198. https://doi.org/10.1016/j.rse.2017.11.022.
Du, Y., Fu, H., Liu, L., Feng, G., Peng, X., Wen, D., 2021. Orbit error removal in InSAR/MTInSAR with a patch-based polynomial model. Int. J. Appl. Earth Obs. Geoinformation 102, 102438. https://doi.org/10.1016/j.jag.2021.102438.
Efron, B., 1982. The jackknife, the bootstrap, and other resampling plans, CBMS-NSF regional conference series in applied mathematics. Society for Industrial and Applied Mathematics.
Emardson, T.R., Simons, M., Webb, F.H., 2003. Neutral atmospheric delay in interferometric synthetic aperture radar applications: statistical description and mitigation. J. Geophys. Res. Solid Earth 108. https://doi.org/10.1029/2002JB001781.
Erban, L.E., Gorelick, S.M., Zebker, H.A., 2014. Groundwater extraction, land subsidence, and sea-level rise in the Mekong Delta. Vietnam. Environ. Res. Lett. 9, 084010 https://doi.org/10.1088/1748-9326/9/8/084010.
Even, M., Schulz, K., 2018. InSAR deformation analysis with distributed scatterers: a review complemented by new advances. Remote Sens. 10, 744. https://doi.org/10.3390/rs10050744.
Falabella, F., Pepe, A., 2022. On the phase nonclosure of multilook SAR interferogram triplets. IEEE Trans. Geosci. Remote Sens. 60, 1–17. https://doi.org/10.1109/TGRS.2022.3216083.
Falabella, F., Serio, C., Zeni, G., Pepe, A., 2020. On the use of weighted least-squares approaches for differential interferometric SAR analyses: the weighted adaptive Variable-lEngth (WAVE) technique. Sensors 20, 1103. https://doi.org/10.3390/s20041103.
Falabella, F., Perrone, A., Stabile, T.A., Pepe, A., 2022a. Atmospheric phase screen compensation on wrapped ground-based SAR interferograms. IEEE Trans. Geosci. Remote Sens. 60, 1–15. https://doi.org/10.1109/TGRS.2021.3055648.
Falabella, F., Serio, C., Masiello, G., Zhao, Q., Pepe, A., 2022b. A multigrid InSAR technique for joint analyses at single-look and multi-look scales. IEEE Geosci. Remote Sens. Lett. 19, 1–5. https://doi.org/10.1109/LGRS.2021.3086271.
Fan, H., Wang, L., Wen, B., Du, S., 2021. A new model for three-dimensional deformation extraction with single-track InSAR based on mining subsidence characteristics. Int. J. Appl. Earth Obs. Geoinformation 94, 102223. https://doi.org/10.1016/j.jag.2020.102223.
Fattahi, H., Amelung, F., 2013. DEM error correction in InSAR time series. IEEE Trans. Geosci. Remote Sens. 51, 4249–4259. https://doi.org/10.1109/TGRS.2012.2227761.
Ferretti, A., Prati, C., Rocca, F., 2001. Permanent scatterers in SAR interferometry. IEEE Trans. Geosci. Remote Sens. 39, 8–20. https://doi.org/10.1109/36.898661.
Ferretti, A., Savio, G., Barzaghi, R., Borghi, A., Musazzi, S., Novali, F., Prati, C., Rocca, F., 2007. Submillimeter accuracy of InSAR time series: experimental validation. IEEE Trans. Geosci. Remote Sens. 45, 1142–1153. https://doi.org/10.1109/TGRS.2007.894440.
Ferretti, A., Fumagalli, A., Novali, F., Prati, C., Rocca, F., Rucci, A., 2011. A new algorithm for processing interferometric data-stacks: SqueeSAR. IEEE Trans. Geosci. Remote Sens. 49, 3460–3470. https://doi.org/10.1109/TGRS.2011.2124465.
Fornaro, G., Pauciullo, A., Reale, D., 2011. A null-space method for the phase unwrapping of multitemporal SAR interferometric stacks. IEEE Trans. Geosci. Remote Sens. 49, 2323–2334. https://doi.org/10.1109/TGRS.2010.2102767.
Fornaro, G., Verde, S., Reale, D., Pauciullo, A., 2015. CAESAR: an approach based on covariance matrix decomposition to improve multibaseline-multitemporal interferometric SAR processing. IEEE Trans. Geosci. Remote Sens. 53, 2050–2065. https://doi.org/10.1109/TGRS.2014.2352853.
Foroughnia, F., Nemati, S., Maghsoudi, Y., Perissin, D., 2019. An iterative PS-InSAR method for the analysis of large spatio-temporal baseline data stacks for land subsidence estimation. Int. J. Appl. Earth Obs. Geoinformation 74, 248–258. https://doi.org/10.1016/j.jag.2018.09.018.
Freedman, D.A., 2006. On the so-called "huber Sandwich estimator" and "robust Standard errors". Am. Stat. 60, 299–302. https://doi.org/10.1198/000313006X152207.
Fruneau, B., Achache, J., Delacourt, C., 1996. Observation and modelling of the Saint-Étienne-de-tinée landslide using SAR interferometry. Tectonophysics 265, 181–190. https://doi.org/10.1016/S0040-1951(96)00047-9.
Ghiglia, D.C., Romero, L.A., 1994. Robust two-dimensional weighted and unweighted phase unwrapping that uses fast transforms and iterative methods. JOSA A 11, 107–117. https://doi.org/10.1364/JOSAA.11.000107.
Goldstein, R.M., Zebker, H.A., Werner, C.L., 1988. Satellite radar interferometry: two-dimensional phase unwrapping. Radio Sci. 23, 713–720. https://doi.org/10.1029/RS023i004p00713.
González, P.J., Fernández, J., 2011. Error estimation in multitemporal InSAR deformation time series, with application to Lanzarote, Canary Islands. J. Geophys. Res. Solid Earth 116. https://doi.org/10.1029/2011JB008412.
Goodman, L.A., 1960. On the exact variance of products. J. Am. Stat. Assoc. 55, 708–713. https://doi.org/10.2307/2281592.
Gourmelen, N., Amelung, F., Casu, F., Manzo, M., Lanari, R., 2007. Mining-related ground deformation in crescent valley, nevada: implications for sparse GPS networks. Geophys. Res. Lett. 34 https://doi.org/10.1029/2007GL029427.
Grandin, R., Klein, E., Métois, M., Vigny, C., 2016. Three-dimensional displacement field of the 2015 Mw8.3 Illapel earthquake (Chile) from across- and along-track Sentinel-1 TOPS interferometry. Geophys. Res. Lett. 43, 2552–2561. https://doi.org/10.1002/2016GL067954.
Guarnieri, A.M., Tebaldini, S., 2008. On the exploitation of target statistics for SAR interferometry applications. IEEE Trans. Geosci. Remote Sens. 46, 3436–3443. https://doi.org/10.1109/TGRS.2008.2001756.
Gudmundsson, S., Sigmundsson, F., Carstensen, J.M., 2002. Three-dimensional surface motion maps estimated from combined interferometric synthetic aperture radar and GPS data. J. Geophys. Res. Solid Earth 107, ETG 13-1-ETG 13-14. 10.1029/2001JB000283.
Guo, H., Jiao, J.J., 2007. Impact of coastal land reclamation on ground water level and the sea water interface. Groundwater 45, 362–367. https://doi.org/10.1111/j.1745-6584.2006.00290.x.
Hanssen, R.F., 2001. Radar Interferometry: Data Interpretation and Error Analysis, Remote Sensing and Digital Image Processing. Springer Netherlands, Dordrecht. 10.1007/0-306-47633-9.
Hilley, G.E., Bürgmann, R., Ferretti, A., Novali, F., Rocca, F., 2004. Dynamics of slow-moving landslides from permanent scatterer analysis. Science 304, 1952–1955. https://doi.org/10.1126/science.1098821.
Hinkley, D.V., 1977. Jackknifing in unbalanced situations. Technometrics 19, 285–292. https://doi.org/10.2307/1267698.
Hooper, A., Zebker, H.A., 2007. Phase unwrapping in three dimensions with application to InSAR time series. JOSA A 24, 2737–2747. https://doi.org/10.1364/JOSAA.24.002737.
Hooper, A., Zebker, H., Segall, P., Kampes, B., 2004. A new method for measuring deformation on volcanoes and other natural terrains using InSAR persistent scatterers. Geophys. Res. Lett. 31 https://doi.org/10.1029/2004GL021737.
Hu, J., Li, Z., Ding, X., Zhu, J., Sun, Q., 2013. Spatial–temporal surface deformation of Los Angeles over 2003–2007 from weighted least squares DInSAR. Int. J. Appl. Earth Obs. Geoinformation 21, 484–492. https://doi.org/10.1016/j.jag.2012.07.007.
Hu, J., Liu, J., Li, Z., Zhu, J., Wu, L., Sun, Q., Wu, W., 2021. Estimating three-dimensional coseismic deformations with the SM-VCE method based on heterogeneous SAR observations: selection of homogeneous points and analysis of observation combinations. Remote Sens. Environ. 255, 112298 https://doi.org/10.1016/j.rse.2021.112298.
Iglesias, R., Fabregas, X., Aguasca, A., Mallorqui, J.J., Lopez-Martinez, C., Gili, J.A., Corominas, J., 2014. Atmospheric phase screen compensation in ground-based SAR with a multiple-regression model over mountainous regions. IEEE Trans. Geosci. Remote Sens. 52, 2436–2449. https://doi.org/10.1109/TGRS.2013.2261077.
Izumi, Y., Nico, G., Sato, M., 2022a. Time-series clustering methodology for estimating atmospheric phase screen in ground-based InSAR data. IEEE Trans. Geosci. Remote Sens. 60, 1–9. https://doi.org/10.1109/TGRS.2021.3072037.
Izumi, Y., Takeuchi, W., Widodo, J., Sulaiman, A., Awaluddin, A., Aditiya, A., Razi, P., Anggono, T., Sumantyo, J.T.S., 2022b. Temporal subset SBAS InSAR approach for tropical peatland Surface deformation monitoring using sentinel-1 data. Remote Sens. 14, 5825. https://doi.org/10.3390/rs14225825.
Jiang, C., Wang, L., Yu, X., 2021. Retrieving 3D Large gradient deformation induced to mining subsidence based on fusion of boltzmann prediction model and single-Track InSAR Earth observation technology. IEEE Access 9, 87156–87172. https://doi.org/10.1109/ACCESS.2021.3089160.
Kirui, P.K., Riedel, B., Gerke, M., 2022. Multi-temporal InSAR tropospheric delay modelling using tikhonov regularization for Sentinel-1 C-band data. ISPRS Open J. Photogramm. Remote Sens. 6, 100020 https://doi.org/10.1016/j.ophoto.2022.100020.
Ku, H.H., 1966. Notes on the use of propagation of error formulas. J. Res. Natl. Bur. Stand. Sect. C Eng. Instrum. 70C, 263. https://doi.org/10.6028/jres.070C.025.
Lauknes, T.R., Zebker, H.A., Larsen, Y., 2011. InSAR deformation time series using an $_1$ -norm small-baseline approach. IEEE Trans. Geosci. Remote Sens. 49, 536–546. https://doi.org/10.1109/TGRS.2010.2051951.

Lee, J.-S., Hoppel, K.W., Mango, S.A., Miller, A.R., 1994. Intensity and phase statistics of multilook polarimetric and interferometric SAR imagery. IEEE Trans. Geosci. Remote Sens. 32, 1017–1028. https://doi.org/10.1109/36.312890.

Lentini, F., Carbone, S., Di Stefano, A., Guarnieri, P., 2002. Stratigraphical and structural constraints in the lucanian apennines (southern Italy): tools for reconstructing the geological evolution. J. Geodyn. 34, 141–158. https://doi.org/10.1016/S0264-3707(02)00031-5.

Leva, D., Nico, G., Tarchi, D., Fortuny-Guasch, J., Sieber, A.J., 2003. Temporal analysis of a landslide by means of a ground-based SAR interferometer. IEEE Trans. Geosci. Remote Sens. 41, 745–752. https://doi.org/10.1109/TGRS.2003.808902.

Li, Y., Jiao, Q., Hu, X., Li, Z., Li, B., Zhang, J., Jiang, W., Luo, Y., Li, Q., Ba, R., 2020. Detecting the slope movement after the 2018 baige landslides based on ground-based and space-borne radar observations. Int. J. Appl. Earth Obs. Geoinformation 84, 101949. https://doi.org/10.1016/j.jag.2019.101949.

Li, Z.W., Yang, Z.F., Zhu, J.J., Hu, J., Wang, Y.J., Li, P.X., Chen, G.L., 2015. Retrieving three-dimensional displacement fields of mining areas from a single InSAR pair. J. Geod. 89, 17–32. https://doi.org/10.1007/s00190-014-0757-1.

Liang, H., Zhang, L., Lu, Z., Li, X., 2023. Correction of spatially varying stratified atmospheric delays in multitemporal InSAR. Remote Sens. Environ. 285, 113382 https://doi.org/10.1016/j.rse.2022.113382.

Liu, J.G., Mason, P., Hilton, F., Lee, H., 2004. Detection of rapid erosion in SE Spain. Photogramm. Eng. Remote Sens. 70, 1179–1185. https://doi.org/10.14358/PERS.70.10.1179.

Lohman, R.B., Simons, M., 2005. Some thoughts on the use of InSAR data to constrain models of surface deformation: noise structure and data downsampling. Geochem. Geophys. Geosystems 6. https://doi.org/10.1029/2004GC000841.

Long, J.S., Ervin, L.H., 2000. Using heteroscedasticity consistent standard errors in the linear regression model. Am. Stat. 54, 217–224. https://doi.org/10.2307/2685594.

Lundgren, P., Berardino, P., Coltelli, M., Fornaro, G., Lanari, R., Puglisi, G., Sansosti, E., Tesauro, M., 2003. Coupled magma chamber inflation and sector collapse slip observed with synthetic aperture radar interferometry on Mt. Etna volcano. J. Geophys. Res. Solid Earth 108. https://doi.org/10.1029/2001JB000657.

MacKinnon, J.G., White, H., 1985. Some heteroskedasticity-consistent covariance matrix estimators with improved finite sample properties. J. Econom. 29, 305–325. https://doi.org/10.1016/0304-4076(85)90158-7.

Maghsoudi, Y., Hooper, A.J., Wright, T.J., Lazecky, M., Ansari, H., 2022. Characterizing and correcting phase biases in short-term, multilooked interferograms. Remote Sens. Environ. 275, 113022 https://doi.org/10.1016/j.rse.2022.113022.

Mardia, K.V., Jupp, P.E. (Eds.), 1999. Directional Statistics, Wiley Series in Probability and Statistics. John Wiley & Sons, Inc., Hoboken, NJ, USA. 10.1002/9780470316979.

Massonnet, D., Feigl, K.L., 1998. Radar interferometry and its application to changes in the Earth's surface. Rev. Geophys. 36, 441–500. https://doi.org/10.1029/97RG03139.

Massonnet, D., Rossi, M., Carmona, C., Adragna, F., Peltzer, G., Feigl, K., Rabaute, T., 1993. The displacement field of the landers earthquake mapped by radar interferometry. Nature 364, 138–142. https://doi.org/10.1038/364138a0.

Mastro, P., Serio, C., Masiello, G., Pepe, A., 2020. The multiple aperture SAR interferometry (MAI) technique for the detection of Large ground displacement dynamics: an overview. Remote Sens. 12, 1189. https://doi.org/10.3390/rs12071189.

Michel, R., Avouac, J.-P., Taboury, J., 1999. Measuring ground displacements from SAR amplitude images: application to the landers Earthquake. Geophys. Res. Lett. 26, 875–878. https://doi.org/10.1029/1999GL900138.

Milillo, P., Rignot, E., Rizzoli, P., Scheuchl, B., Mouginot, J., Bueso-Bello, J., Prats-Iraola, P., 2019. Heterogeneous retreat and ice melt of thwaites glacier. West Antarctica. Sci. Adv. 5, eaau3433. https://doi.org/10.1126/sciadv.aau3433.

Monserrat, O., Crosetto, M., Luzi, G., 2014. A review of ground-based SAR interferometry for deformation measurement. ISPRS J. Photogramm. Remote Sens. 93, 40–48. https://doi.org/10.1016/j.isprsjprs.2014.04.001.

Mora, O., Mallorqui, J.J., Broquetas, A., 2003. Linear and nonlinear terrain deformation maps from a reduced set of interferometric SAR images. IEEE Trans. Geosci. Remote Sens. 41, 2243–2253. https://doi.org/10.1109/TGRS.2003.814657.

Othman, A., Abotalib, A.Z., 2019. Land subsidence triggered by groundwater withdrawal under hyper-arid conditions: case study from Central Saudi Arabia. Environ. Earth Sci. 78, 243. https://doi.org/10.1007/s12665-019-8254-8.

Pepe, A., 2021. Multi-temporal small baseline interferometric SAR algorithms: error budget and theoretical performance. Remote Sens. 13, 557. https://doi.org/10.3390/rs13040557.

Pepe, A., Calò, F., 2017. A review of interferometric synthetic aperture RADAR (InSAR) multi-track approaches for the retrieval of Earth's surface displacements. Appl. Sci. 7, 1264. https://doi.org/10.3390/app7121264.

Pepe, A., Lanari, R., 2006. On the extension of the minimum cost flow algorithm for phase unwrapping of multitemporal differential SAR interferograms. IEEE Trans. Geosci. Remote Sens. 44, 2374–2383. https://doi.org/10.1109/TGRS.2006.873207.

Pepe, A., Solaro, G., Calò, F., Dema, C., 2016. A minimum acceleration approach for the retrieval of multiplatform InSAR deformation time series. IEEE J Sel. Top. Appl. Earth Obs. Remote Sens. 9, 3883–3898. https://doi.org/10.1109/JSTARS.2016.2577878.

Perissin, D., Wang, Z., Lin, H., 2012. Shanghai subway tunnels and highways monitoring through cosmo-SkyMed persistent scatterers. ISPRS J. Photogramm. Remote Sens Innovative Applications of SAR Interferometry from Modern Satellite Sensors 73, 58–67. https://doi.org/10.1016/j.isprsjprs.2012.07.002.

Pritchard, M.E., Simons, M., 2004. An InSAR-based survey of volcanic deformation in the central Andes. Geochem. Geophys. Geosystems 5. https://doi.org/10.1029/2003GC000610.

Pritt, M.D., 1996. Phase unwrapping by means of multigrid techniques for interferometric SAR. IEEE Trans. Geosci. Remote Sens. 34, 728–738. https://doi.org/10.1109/36.499752.

Qiu, Z., Ma, Y., Guo, X., 2016. Atmospheric phase screen correction in ground-based SAR with PS technique. Springerplus 5, 1594. https://doi.org/10.1186/s40064-016-3262-6.

Ramsey, J.B., 1969. Tests for specification errors in classical linear least-Squares regression analysis. J. r. Stat. Soc. Ser. B Methodol. 31, 350–371.

Rocca, F., 2007. Modeling interferogram stacks. IEEE Trans. Geosci. Remote Sens. 45, 3289–3299. https://doi.org/10.1109/TGRS.2007.902286.

Rödelsperger, S., Becker, M., Gerstenecker, C., Läufer, G., Schilling, K., Steineck, D., 2010. Digital elevation model with the ground-based SAR IBIS-L as basis for volcanic deformation monitoring. J. Geodyn. 49, 241–246. https://doi.org/10.1016/j.jog.2009.10.009.

Samiei-Esfahany, S., Hanssen, R., 2017. On the evaluation of second order phase statistics in SAR interferogram stacks. Earth Obs. Geomat. Eng. 1 https://doi.org/10.22059/eoge.2017.63865.1016.

Samsonov, S., 2010. Topographic correction for ALOS PALSAR interferometry. IEEE Trans. Geosci. Remote Sens. 48, 3020–3027. https://doi.org/10.1109/TGRS.2010.2043739.

Samsonov, S., d'Oreye, N., 2012. Multidimensional time-series analysis of ground deformation from multiple InSAR data sets applied to virunga volcanic province. Geophys. J. Int. 191, 1095–1108. https://doi.org/10.1111/j.1365-246X.2012.05669.x.

Samsonov, S., Tiampo, K., Rundle, J., Li, Z., 2007. Application of DInSAR-GPS optimization for derivation of fine-scale surface motion maps of Southern California. IEEE Trans. Geosci. Remote Sens. 45, 512–521. https://doi.org/10.1109/TGRS.2006.887166.

Samsonov, S., d'Oreye, N., Smets, B., 2013. Ground deformation associated with post-mining activity at the french-german border revealed by novel InSAR time series method. Int. J. Appl. Earth Obs. Geoinformation 23, 142–154. https://doi.org/10.1016/j.jag.2012.12.008.

Sandwell, D.T., Sichoix, L., Agnew, D., Bock, Y., Minster, J.-B., 2000. Near real-time radar interferometry of the mw 7.1 Hector mine Earthquake. Geophys. Res. Lett. 27, 3101–3104. https://doi.org/10.1029/1999GL011209.

Schlögel, R., Doubre, C., Malet, J.-P., Masson, F., 2015. Landslide deformation monitoring with ALOS/PALSAR imagery: a D-InSAR geomorphological interpretation method. Geomorphology 231, 314–330. https://doi.org/10.1016/j.geomorph.2014.11.031.

Shaffer, J.P., 2012. The gauss—markov theorem and random regressors. Am. Stat.

Shanker, A.P., Zebker, H., 2010. Edgelist phase unwrapping algorithm for time series InSAR analysis. JOSA A 27, 605–612. https://doi.org/10.1364/JOSAA.27.000605.

Smith, L.C., Alsdorf, D.E., Magilligan, F.J., Gomez, B., Mertes, L.A.K., Smith, N.D., Garvin, J.B., 2000. Estimation of erosion, deposition, and net volumetric change caused by the 1996 Skeiðarársandur jökulhlaup, Iceland, from synthetic aperture Radar interferometry. Water Resour. Res. 36, 1583–1594. https://doi.org/10.1029/1999WR900335.

Strozzi, T., Antonova, S., Günther, F., Mätzler, E., Vieira, G., Wegmüller, U., Westermann, S., Bartsch, A., 2018. Sentinel-1 SAR interferometry for surface deformation monitoring in low-land permafrost areas. Remote Sens. 10, 1360. https://doi.org/10.3390/rs10091360.

Takahashi, K., Matsumoto, M., Sato, M., 2013. Continuous observation of natural-disaster-affected areas using ground-based SAR interferometry. IEEE J Sel. Top. Appl. Earth Obs. Remote Sens. 6, 1286–1294. https://doi.org/10.1109/JSTARS.2013.2249497.

Tang, M., Zhao, Q., Pepe, A., Devlin, A.T., Falabella, F., Yao, C., Li, Z., 2022. Changes of chinese coastal regions induced by land reclamation as revealed through TanDEM-X DEM and InSAR analyses. Remote Sens. 14, 637. https://doi.org/10.3390/rs14030637.

Tarchi, D., Casagli, N., Fanti, R., Leva, D.D., Luzi, G., Pasuto, A., Pieraccini, M., Silvano, S., 2003. Landslide monitoring by using ground-based SAR interferometry: an example of application to the tessina landslide in Italy. Eng. Geol Remote Sensing and Monitoring of Landslides 68, 15–30. https://doi.org/10.1016/S0013-7952(02)00196-5.

Tian, X., Malhotra, R., Xu, B., Qi, H., Ma, Y., 2018. Modeling orbital error in InSAR interferogram using frequency and spatial domain based methods. Remote Sens. 10, 508. https://doi.org/10.3390/rs10040508.

Tizzani, P., Berardino, P., Casu, F., Euillades, P., Manzo, M., Ricciardi, G.P., Zeni, G., Lanari, R., 2007. Surface deformation of long valley caldera and mono basin, california, investigated with the SBAS-InSAR approach. Remote Sens. Environ. 108, 277–289. https://doi.org/10.1016/j.rse.2006.11.015.

Tough, J.A., Blacknell, D., Quegan, S., 1995. A statistical description of polarimetric and interferometric synthetic aperture radar data. Proc. r. Soc. Lond. Ser. Math. Phys. Sci. 449, 567–589. https://doi.org/10.1098/rspa.1995.0059.

Wang, Z., Hu, J., Chen, Y., Liu, X., Liu, J., Wu, W., Wang, Y., 2022. Integration of ground-based and space-borne radar observations for three-dimensional deformations reconstruction: application to luanchuan mining area. China. Geomat. Nat. Hazards Risk 13, 2819–2839. https://doi.org/10.1080/19475705.2022.2134828.

Wang, P., Xing, C., Pan, X., 2020. Reservoir dam Surface deformation monitoring by differential GB-InSAR based on image subsets. Sensors 20, 396. https://doi.org/10.3390/s20020396.

White, H., 1980. A heteroskedasticity-consistent covariance matrix estimator and a direct test for heteroskedasticity. Econometrica 48, 817–838. https://doi.org/10.2307/1912934.

Wright, T.J., Parsons, B.E., Lu, Z., 2004. Toward mapping surface deformation in three dimensions using InSAR. Geophys. Res. Lett. 31 https://doi.org/10.1029/2003GL018827.

Xiao, T., Huang, W., Deng, Y., Tian, W., Sha, Y., 2021. Long-term and emergency monitoring of zhongbao landslide using space-borne and ground-based InSAR. Remote Sens. 13, 1578. https://doi.org/10.3390/rs13081578.

Yang, Z., Li, Z., Zhu, J., Yi, H., Hu, J., Feng, G., 2017. Deriving dynamic subsidence of coal mining areas using InSAR and logistic model. Remote Sens. 9, 125. https://doi.org/10.3390/rs9020125.

Zebker, H.A., Villasenor, J., 1992. Decorrelation in interferometric radar echoes. IEEE Trans. Geosci. Remote Sens. 30, 950–959. https://doi.org/10.1109/36.175330.

Zhao, Q., Pan, J., Devlin, A.T., Tang, M., Yao, C., Zamparelli, V., Falabella, F., Pepe, A., 2022. On the exploitation of remote sensing technologies for the monitoring of coastal and river delta regions. Remote Sens. 14, 2384. https://doi.org/10.3390/rs14102384.

Zheng, Y., Zebker, H., Michaelides, R., 2021. A new decorrelation phase covariance model for noise reduction in unwrapped interferometric phase stacks. IEEE Trans. Geosci. Remote Sens. 59, 10126–10135. https://doi.org/10.1109/TGRS.2021.3050087.

Zheng, Y., Fattahi, H., Agram, P., Simons, M., Rosen, P., 2022. On closure phase and systematic bias in multilooked SAR interferometry. IEEE Trans. Geosci. Remote Sens. 60, 1–11. https://doi.org/10.1109/TGRS.2022.3167648.